nature biotechnology

Article

https://doi.org/10.1038/s41587-026-03140-1

Fetal monitoring for high-risk pregnancies using a wearable ultrasound patch

Received: 25 September 2025

Accepted: 21 April 2026

Published online: 26 May 2026

Check for updates

Geonho Park[1,2,12], Yizhou Bian[1,12], Hao Huang[1,12], Sai Zhou[3,12], Siyu Qin[4], Muyang Lin[1], Xinyi Yang[3], Aaron Lee[5], Anand Ramkumar[6], Mariana Tome[6], Jayne Lander[6], Xiangjun Chen[2,3], Shenghan Wang[1], Pranavi Bheemreddy[4], Liam Stanton[1], Ren Sheng[7], Guihuan Guo[1], Mabel Shehada[5], Ruotao Wang[1], Alexa Roa[5], Chengchangfeng Lu[4], Wentong Yue[1], Ray S. Wu[1], Xiaoxiang Gao[1], Hongjie Hu[1], Amer Yaghi[1], Mark Liu[8], Lawrence Impey[6], Sally L. Collins[6], Aris T. Papageorghiou[6], Louise C. Laurent[9], Keith A. Wear[10], Antoniya Georgieva[6] ✉ & Sheng Xu[1,2,3,4,5,11] ✉

Ultrasonography is widely used for fetal monitoring but it requires sonographers and is limited to snapshot evaluations at discrete intervals. Here we report a wearable ultrasound patch (UPatch) for continuous and autonomous fetal monitoring. The UPatch can acquire anatomical structures and blood flow velocities, demonstrating good agreement with a handheld clinical ultrasound device on 62 pregnancies. Real-time image segmentation allows autonomous tracking of target vessels to acquire continuous blood flow spectra during fetal and maternal movements without a sonographer. Continuous monitoring data from 52 pregnant women aligned with stratified perinatal conditions, including healthy, small for gestational age, large for gestational age, gestational diabetes, preeclampsia and gestational hypertension. With further technology development, integration with a miniaturized circuit could enable fully wireless operation and greater user mobility. The UPatch could provide continuous assessment of fetal compromise in high-risk pregnancies, expanding prenatal-care capabilities.

The physiological maturation of the fetus in the uterus is supported by coordinated blood flow through the maternal, placental and fetal circulations[1]. Any disruption of these hemodynamic interactions can precipitate fetal complications, such as hypoxia[2], intrauterine growth restriction[3] and cerebral palsy[4], with stillbirth[5] being the most extreme outcome. Despite decades of research, many such fetal complications remain undiagnosed and unexplained, with existing methods relying mostly on postmortem investigations[6,7]. Continuous monitoring of fetal anatomy and hemodynamics throughout pregnancy not only provides insights into the pathophysiological mechanisms of fetal complications but also allows early detection and mitigation of emerging issues, helping to prevent adverse outcomes (Supplementary Discussion 1)[8,9].

Continuous fetal monitoring currently relies predominantly on cardiotocography, which measures the fetal heart rate and uterine contractions (Supplementary Fig. 1 and Supplementary Discussion 2)[10,11]. However, given the complexity of fetal physiology, these measurements do not correlate well with fetal health and yield false-positive rates up to 50% (Supplementary Discussion 3)[12–15]. Other continuous monitoring devices based on electrocardiography[16], pulse oximetry[17] or accelerometry[18] cannot reliably differentiate fetal from maternal signals and are not commonly used in clinical practice. Ultrasonography is widely used to measure fetal biometry and blood flow (Supplementary Discussion 4)[19–21] and standardized reference indices have been established throughout gestation to evaluate fetal health (Supplementary Discussion 5)[22–25]. However, conventional ultrasonography is heavily dependent on the skills of the operator and measurements are limited to snapshots that can fail to capture the longitudinal patterns and critical moments

A full list of affiliations appears at the end of the paper. ✉e-mail: antoniya.georgieva@wrh.ox.ac.uk; shengxu@stanford.edu

https://doi.org/10.1038/s41587-026-03140-1

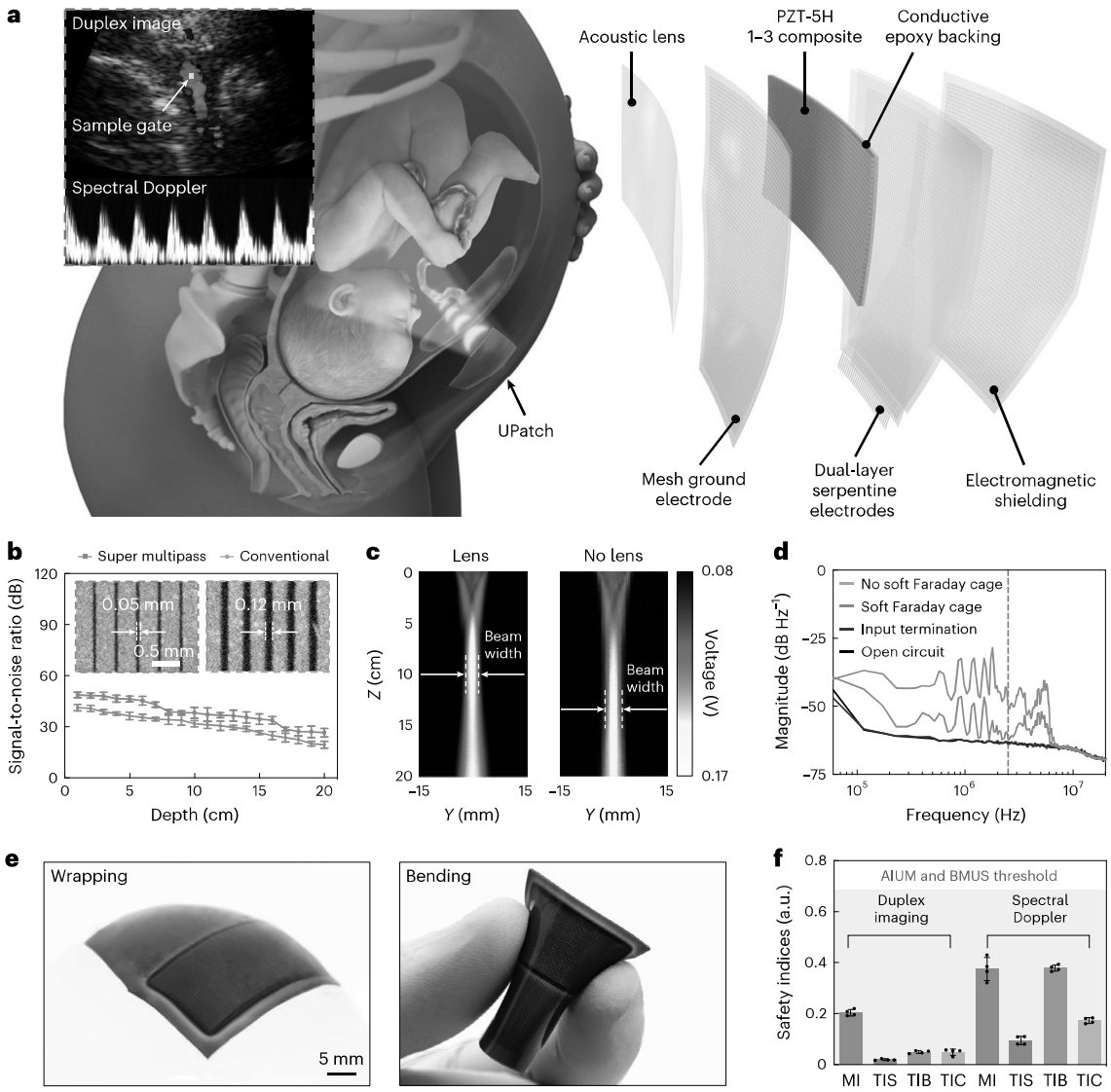

Fig. 1 | Overview of the UPatch. a, Schematics of the working principle of the UPatch for fetal monitoring (left) and a structurally exploded view (right). The UPatch is attached to the maternal abdomen to monitor fetal anatomical structures and hemodynamics continuously with duplex imaging. A sample gate, indicated by the green dot, defines the target region for blood flow measurements from a fetal vessel. A diverging beam is used for imaging and a focused beam is used for blood flow measurement. The UPatch is multilayered to enhance its signals and minimize its form factors. **b**, Comparison of signal-to-noise ratios between transducers diced with the conventional method and the super multipass method ($n = 12$). Insets, optical images showing the results from the two dicing methods. The images share the same scale bar. **c**, Acoustic fields measured using a hydrophone in the elevational plane of the UPatch with (left) and without (right) an acoustic lens. **d**, The power spectral density analysis of the UPatch with and without the soft Faraday cage, input termination at 50 Ω and open circuit of the backend system. The soft Faraday cage reduces noise coupling from electromagnetic interference by 11.7 dB Hz^{-1} at 2.5 MHz (gray dashed line), the center frequency of the UPatch. **e**, Photographs of the UPatch demonstrating its mechanical compliance in wrapping (left) and bending (right) shapes. Images share the same scale bar. **f**, UPatch safety measurements. The mechanical index (MI), soft tissue thermal index (TIS), bone thermal index (TIB) and cranium thermal index (TIC) were all well below the thresholds of 0.7 recommended by the American Institute of Ultrasound in Medicine (AIUM)[41] and British Medical Ultrasound Society (BMUS)[42] guidelines for continuous monitoring ($n = 4$). Data in **b**,**f** are presented as the mean ± s.d.

of fetal hemodynamics[26,27]. Although wearable ultrasound devices have been developed for continuous monitoring of physiological signals[28–31], they are unsuitable for fetal monitoring because of weak blood flow signals from deep fetal vessels and signal loss during large fetal movements.

Here, we report a wearable ultrasound patch (UPatch) that can continuously image the fetus and autonomously measure fetal blood flow in real time (Supplementary Discussion 6). To enhance the signal-to-noise ratio and imaging resolution, we integrated transducers fabricated by super multipass dicing, as well as an acoustic lens and a soft Faraday cage (Extended Data Fig. 1). To identify and track moving targets, we used a segmentation-based algorithm to place sample gates in the duplex images. Blood flow spectra can be acquired continuously and autonomously in real time, even during large fetal movements. We conducted a prospective study with 62 pregnant participants to validate the accuracy of the UPatch compared with a handheld clinical ultrasound device. Furthermore, we used the UPatch to continuously monitor the umbilical cord blood flow in 52 participants, generating longitudinal measurements that distinguished transient fluctuations from sustained compromise. We found that Doppler indices exhibited monotonic relationship with gestational age and differentiated high-risk from healthy pregnancies. In a preeclamptic case, the UPatch revealed the severity of intrauterine growth restriction, leading to an early Cesarian delivery to prevent stillbirth.

https://doi.org/10.1038/s41587-026-03140-1

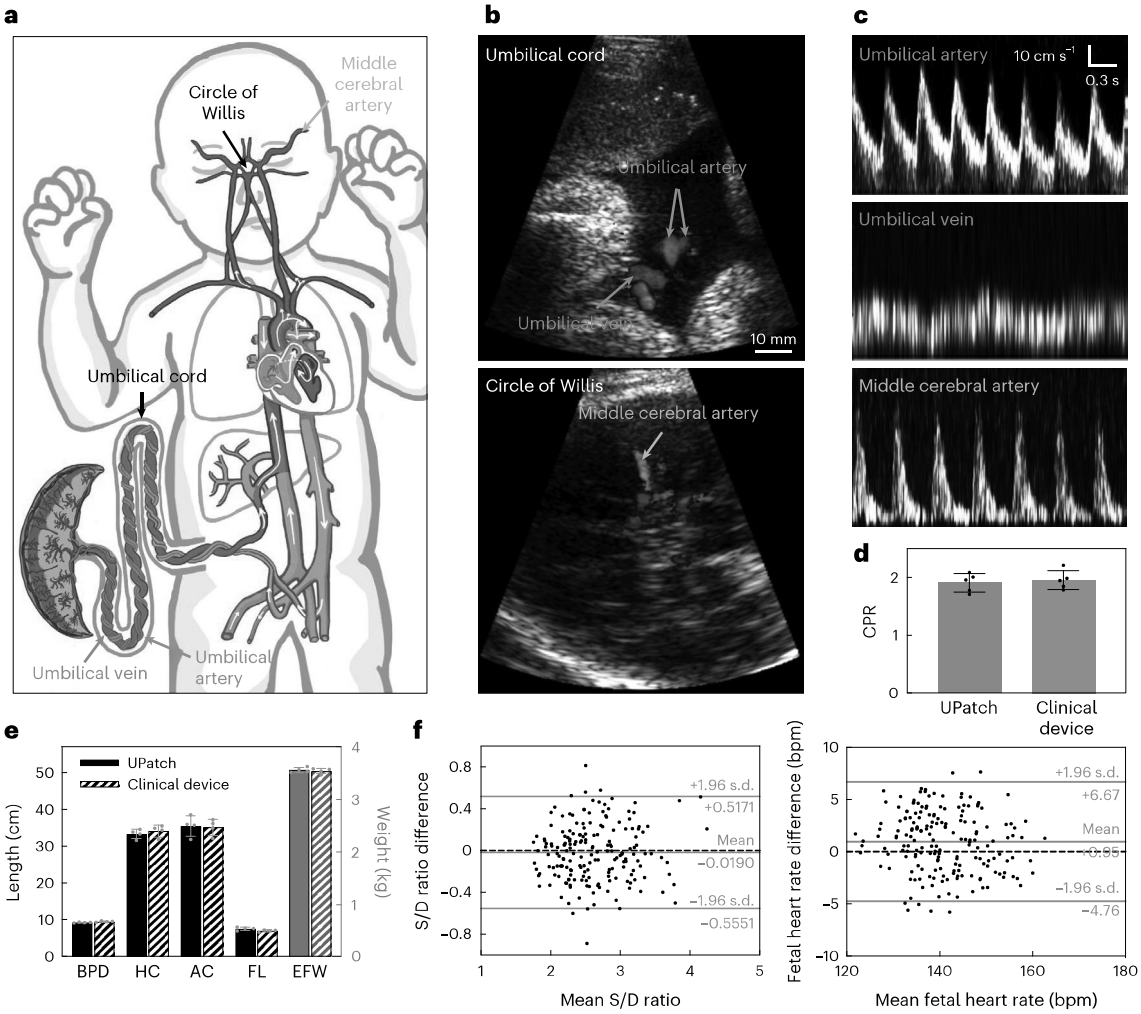

Fig. 2 | Measurements and validations of the UPatch for fetal monitoring. **a**, Schematics illustrating the fetal cardiovascular system. The umbilical cord shows coiling of the two umbilical arteries and one umbilical vein. The middle cerebral artery is located within the circle of Willis. **b**, Duplex images of the umbilical cord and circle of Willis recorded with the UPatch. The images share the same scale bar. **c**, Blood flow spectra from three key vessels recorded with the UPatch. The spectra share the same scale bar. **d**, Comparison of the cerebroplacental ratio (CPR) measured with the UPatch and a handheld clinical ultrasound device (Voluson E10, GE Healthcare) ($n = 5$). **e**, Comparison of fetal biometry measured with the UPatch and a handheld clinical ultrasound device. Biparietal diameter (BPD), head circumference (HC), abdominal circumference (AC) and femur length (FL) were used to calculate fetal weight (EFW) ($n = 4$)[48]. **f**, Bland–Altman plots for the systolic-to-diastolic ratio (S/D ratio; left) and fetal heart rate in beats per minute (bpm) (right) measured using the UPatch and a handheld clinical ultrasound device. Solid red lines are the mean differences between the two devices, solid blue lines are 95% limits of agreement (1.96 s.d. above and below the mean differences) and black dashed lines are the zero difference between the two devices. Each plot includes three repeated measurement pairs acquired using the same devices in each of the 62 participants. Data in **d**,**e** are presented as the mean ± s.d.

Design of the UPatch

Fetal structures and vessels vary in size and are distributed across a wide range of depths within the uterus (Fig. 1a, left)[32]. Brightness-mode imaging is based on echoes from tissue interfaces and distributed scattering within tissues[33]. In contrast, color Doppler imaging and spectral Doppler waveforms of blood flow are based on the much weaker echoes from red blood cells[33,34].

We adopted three strategies to strengthen the echoes from red blood cells in deep fetal vessels. First, the UPatch contains a 2.5-MHz PZT-5H 1–3 composite with a conductive epoxy backing layer at a pitch of 0.65 ultrasound wavelength (Fig. 1a, right). We used super multipass dicing, which reduced the kerf and, thus, increased the element width by 25% (Fig. 1b, Methods, Supplementary Figs. 2 and 3 and Supplementary Discussion 7). This improved the signal-to-noise ratio by 7.2 dB without increasing the crosstalk between adjacent elements (Supplementary Fig. 4). Second, we designed an acoustic lens to improve elevational focusing, which reduced the focal beamwidth by 25% and, thus, enhanced the spatial resolution and color Doppler signal sensitivity (Fig. 1c, Methods, Supplementary Figs. 5–8 and Supplementary Discussion 8)[35]. Additionally, the acoustic lens moved the elevational focal depth from 14 to 10 cm, on par with clinical devices, to balance the spatial resolution throughout the entire uterus (Fig. 1c and Supplementary Fig. 7). Third, we developed a soft Faraday cage by connecting the electromagnetic shielding layer to the mesh ground electrode layer using vertical interconnect accesses (Methods, Supplementary Figs. 9 and 10 and Supplementary Discussion 9). The cage fully encapsulated the elements and reduced the electromagnetic interference by 11.7 dB Hz^{-1} (Fig. 1d and Supplementary Figs. 11–13)[36]. Additionally, we used two signal electrode layers that can individually address each element with a minimal electrode footprint (Supplementary Fig. 9). The UPatch was mechanically compliant (Fig. 1e) and imposed negligible constraints on the movement of pregnant participants in various positions (Supplementary Fig. 14).

https://doi.org/10.1038/s41587-026-03140-1

Table 1 | Participant demographics in the validation study

Race/ethnicity	*n* (percentage)
White	45 (72.6%)
Asian	5 (8.1%)
Mixed, American Indian	8 (12.9%)
Unknown*	4 (6.4%)
At the time of study	**Mean ± s.d.**
Age (years)	31.45 ± 4.88
Height (cm)	164.44 ± 7.34
Weight (kg)	73.33 ± 18.11
Body mass index	27.17 ± 6.92
Gestational age (days)	238.90 ± 26.68
Placental location	***n* (percentage)**
Anterior	36 (58.1%)
Posterior	17 (27.4%)
Lateral	4 (6.5%)
Fundal	5 (8.1%)

*The participants refused to provide this information.

To quantify the UPatch performance, we characterized its brightness, color Doppler and spectral Doppler modes following the Institute of Physics and Engineering in Medicine protocol (Methods)[37]. On a phantom filled with monofilament wires and tissue-mimicking contrast targets, the axial and lateral resolutions as well as dynamic range and contrast-to-noise ratio of the UPatch in brightness mode were comparable to those of a handheld clinical ultrasound device (Supplementary Fig. 15)[38]. On a flow phantom with blood-mimicking fluids, the color Doppler sensitivity and the spectral Doppler accuracy of the UPatch at different depths and velocities were similar to those of the clinical device (Supplementary Figs. 16 and 17)[39]. On a customized umbilical cord flow phantom, the UPatch reliably acquired flow signals regardless of phantom orientation (Extended Data Fig. 2, Supplementary Figs. 18 and 19 and Supplementary Discussion 10). On a healthy adult participant, all three modes of the UPatch and the clinical device were comparable in quality (Supplementary Figs. 20 and 21).

Acoustic safety characterizations

Minimal acoustic intensity is necessary for the fetus to avoid potential side effects associated with ultrasound exposure[40]. We examined the biological effects of the UPatch in vitro in all three ultrasound modes following the guidelines from the American Institute of Ultrasound in Medicine (AIUM)[41], British Medical Ultrasound Society (BMUS)[42] and Food and Drug Administration (FDA)[43] (Methods and Supplementary Discussion 11). The maximum spatial average temporal average intensity was 0.72 mW cm^{-2} (<20 mW cm^{-2} is recommended by the FDA[43] and 5 mW cm^{-2} is the value reported for the GE Corometrics 250CX (https://my.getzhealthcare.com/getzhealthcare/products/ge-healthcare/corometrics-250cx/corometrics250cx_datasheet.pdf). The maximum derated spatial peak pulse average intensity was 16.42 W cm^{-2} (<190 W cm^{-2} is recommended by the FDA[43]), the maximum derated spatial peak temporal average intensity was 58.5 mW cm^{-2} (<94 mW cm^{-2} is recommended by the FDA[43]) and the mechanical index was 0.20 for duplex (combined brightness and color Doppler) imaging and 0.38 for spectral Doppler (<1.9 is recommended by the FDA[43] and ≤0.7 is recommended by the BMUS[42]) (Fig. 1f).

We also evaluated the thermal characteristics of the UPatch (Supplementary Discussion 12)[44,45]. Surface temperatures were measured using a thermocouple on a phantom and in air (Methods). In both conditions, the temperature increase was <0.7 °C during 48 h of continuous UPatch activation (Supplementary Fig. 22). To calculate the thermal index, acoustic power was measured and cross-checked using a hydrophone and radiation force balance (Methods and Supplementary Figs. 23 and 24)[45]. The soft tissue thermal index, bone thermal index and cranium thermal index were 0.02, 0.05 and 0.05 for duplex imaging and 0.1, 0.38 and 0.17 for spectral Doppler, respectively (Fig. 1f). All measurements were well below the maximum level of 0.7 recommended by the AIUM and BMUS for continuous monitoring[41,42].

Fetal monitoring and validation

Duplex imaging can reveal fetal anatomical abnormalities, quantify fetal biometry and facilitate the recording of spectral Doppler waveforms of fetal vessels[46]. Correcting the phase aberration induced by the maternal abdomen allowed the acquisition of high-quality signals from the UPatch (Supplementary Fig. 25 and Supplementary Discussion 13). The UPatch was able to image the two arteries and one vein in the helical umbilical cord and the middle cerebral artery from the circle of Willis (Fig. 2a,b). Detailed blood flow velocity waveforms were acquired from all of these vessels (Fig. 2c and Supplementary Discussion 5). The cerebroplacental ratio (the pulsatility index of the middle cerebral artery divided by that of the umbilical artery) quantifies the fetal brain-sparing effect during prolonged hypoxia or in placental insufficiency, and the measurements acquired by the UPatch and a clinical device were comparable (Fig. 2d)[47]. The UPatch accurately measured anatomical structures (such as the biparietal diameter (BPD), head circumference (HC), abdominal circumference (AC) and femur length (FL)), providing an estimated fetal weight (EFW) for the assessment of growth-related complications (Fig. 2e, Methods and Supplementary Fig. 26)[48].

The UPatch accuracy was validated against a clinical device on 62 participants across a range of vessel depths, orientations and placental locations (Table 1, Methods, Extended Data Fig. 3 and Supplementary Figs. 27 and 28). From the spectral Doppler waveforms, an envelope extraction algorithm can derive peak-systolic velocity, end-diastolic velocity and fetal heart rate to calculate the systolic-to-diastolic ratio, pulsatility index and resistance index (Supplementary Fig. 29)[49]. Based on Bland–Altman analysis, the mean differences ± s.d. between the UPatch and clinical device were −0.019 ± 0.274 for the systolic-to-diastolic ratio (−0.72% relative mean difference), −0.010 ± 0.117 for the pulsatility index (−0.92%), −0.004 ± 0.044 for the resistance index (−0.64%) and 0.95 ± 2.91 beats per minute (bpm) for the fetal heart rate (0.68%) (Fig. 2f and Supplementary Fig. 30). Pearson correlation coefficients demonstrated a strong linear relationship between the measurements from two devices (Extended Data Fig. 4).

Autonomous vessel tracking

Spectral Doppler waveforms of the umbilical blood flow can monitor the fetoplacental circulation responsible for fetal oxygen and nutrient delivery (Supplementary Discussions 4 and 5)[3]. However, the umbilical cord is a moving target because of fetal and maternal movements, respiration and uterine contractions (Supplementary Discussion 14)[21]. In clinical practice, sonographers manually adjust the color-flow box and set a sample gate to acquire spectral Doppler signals from the target vessel, which is both time-consuming and operator dependent (Supplementary Fig. 31)[50]. In low-resource settings where the incidence of pregnancy complications remains high, such sonographers are often limited in number[51,52].

To reduce the need for manual operation and the corresponding healthcare burden, we developed an image segmentation-based algorithm that can autonomously identify and track moving vessels (Fig. 3a and Supplementary Discussion 15). We used a diverging beam to cover a large field of view, ensuring that the moving vessel remains consistently visible within the ultrasonographic window (Supplementary Fig. 32)[53]. The UPatch stably acquired the umbilical cord signals without repositioning across common maternal postures

https://doi.org/10.1038/s41587-026-03140-1

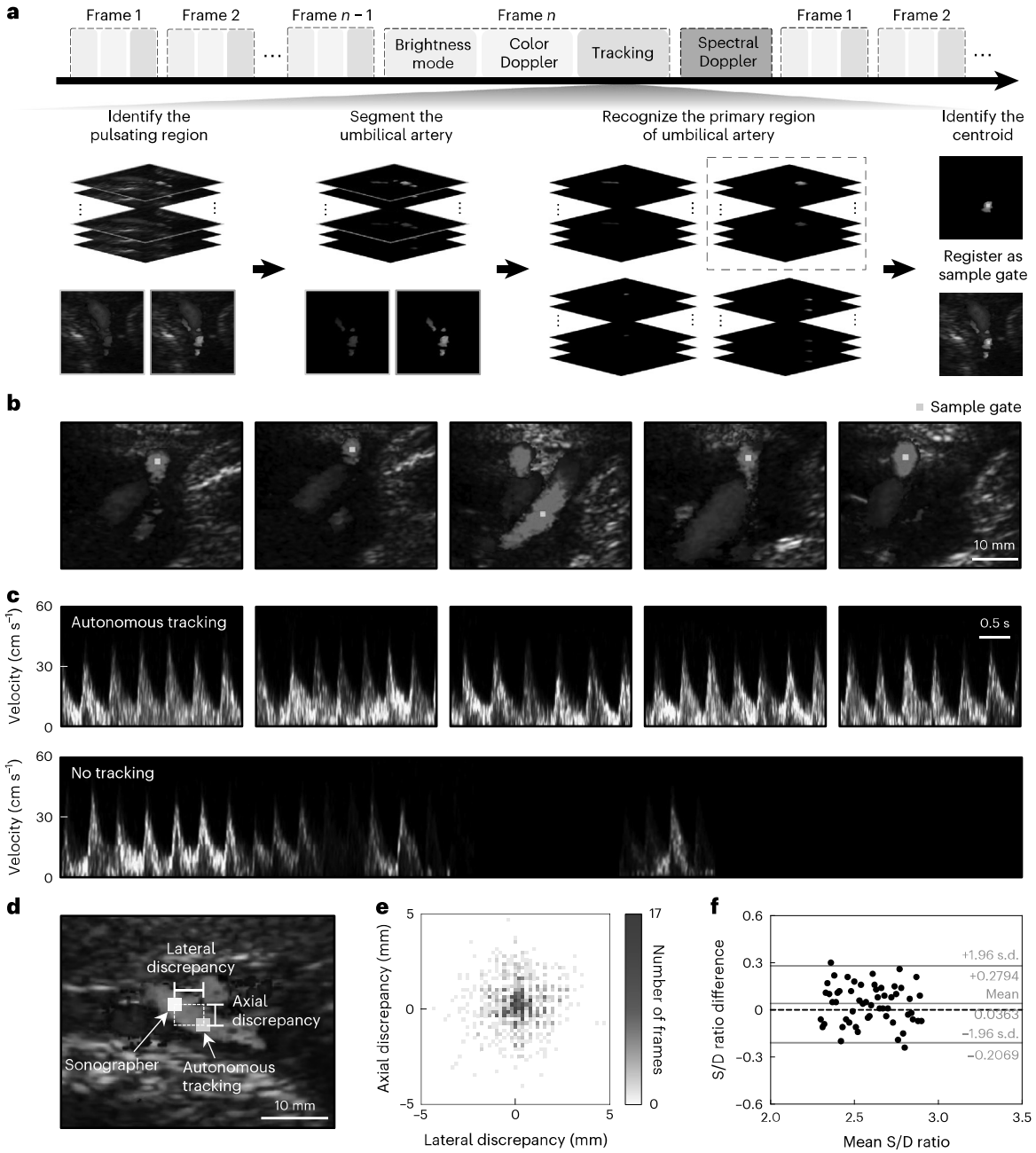

Fig. 3 | Autonomous vessel tracking by image segmentation. a, Beam-forming sequence and working principle of the image segmentation-based vessel-tracking algorithm. Top, the tracking algorithm operates between the duplex imaging and spectral Doppler. Bottom, the algorithm identifies the pulsating regions in consecutive frames, segments the umbilical artery, recognizes the primary region and registers the spatial centroid as the sample gate. Images outlined in green and orange represent the end diastole and peak systole, respectively. In these two images, the blue regions show similar intensities, indicating the non-pulsatile umbilical vein, whereas the red regions show intensity differences, indicating the pulsatile umbilical artery. Among the four segmented areas, the primary region is defined as the largest segmented area (denoted with the black dashed box). **b**, Tracking a moving umbilical artery and registering a sample gate using the UPatch with the autonomous algorithm. All images share the same scale bar. **c**, Top, the autonomous algorithm allows the measurement of blood flow from a moving vessel continuously. Bottom, without the autonomous tracking algorithm, a predefined sample gate results in signal loss because of vessel movements. The spectra share the same scale bar. **d**, A representative image showing the difference between the sample gates labeled by the autonomous tracking algorithm and by a sonographer. **e**, Summary of the lateral and axial discrepancies in the sample gates labeled by the autonomous tracking algorithm and by a sonographer. **f**, Bland–Altman plot for the S/D ratios measured by the autonomous tracking algorithm and a sonographer. The solid red line is the mean difference between the two methods, the solid blue lines are 95% limits of agreement (1.96 s.d. above and below the mean differences) and the black dashed line is the zero difference between the two methods.

(Extended Data Fig. 5). By segmenting the reconstructed duplex images, the tracking algorithm identifies pulsatile signals by calculating the variance in color Doppler pixel intensity across consecutive frames (Fig. 3a, Extended Data Fig. 6 and Supplementary Discussion 16). Then, the algorithm identifies the primary region of the pulsatile signals and registers the spatial centroid of the primary region as the sample gate, where a focused beam is directed to acquire blood flow spectra (Fig. 3a and Supplementary Figs. 33 and 34)[53]. This autonomous sample gate registration enabled continuous blood flow monitoring of a moving vessel in real time (Fig. 3b,c, Supplementary Video 1 and

Supplementary Discussion 17). Without the tracking algorithm, blood flow signals were lost during vessel movements (Fig. 3c).

To validate the accuracy of the autonomous tracking algorithm, we compared its sample gates to those registered by a sonographer in a double-blind test (Fig. 3d, Methods and Supplementary Discussion 18). We found that 91.9% and 90.5% of the sample gates were within a 2-mm discrepancy (an accepted clinical standard) in the lateral and axial directions, respectively (Fig. 3e and Supplementary Discussion 19)[46]. In a separate test, the sample gates registered by the tracking algorithm were considered accurate by three sonographers in 94.2% of the images acquired using the clinical device (with some images affected by fast cord movements) and in 91.2% of the images acquired using the UPatch (because of slight differences in image quality; Methods, Extended Data Fig. 7 and Supplementary Discussion 18). We used Bland–Altman analysis to compare the systolic-to-diastolic ratio from the sample gates acquired by the tracking algorithm and a sonographer (Methods and Supplementary Discussion 18). The mean difference ± s.d. was only 0.036 ± 0.124 (Fig. 3f). While its accuracy was comparable to that of U-Net[54] and ConvLSTM[55], our tracking algorithm achieved more than a tenfold reduction in processing time, enabling real-time image processing (Supplementary Fig. 35 and Supplementary Discussion 18).

Continuous monitoring of pregnant participants

The continuous monitoring of umbilical artery blood flow is important for assessing fetal growth restriction (Supplementary Discussions 4 and 5)[56]. Abnormal waveforms (such as absent or reversed end-diastolic velocities) often indicate fetal pathology because of placental insufficiency and even subtler abnormalities (such as increased Doppler indices) indicate an elevated risk[57,58]. Continuous monitoring of these changes can inform optimal delivery time, managing the competing risks of premature birth, which may lead to postnatal complications[59], and delayed birth, which heightens the risk of asphyxia, cerebral palsy and stillbirth[60].

We used the UPatch to compare a healthy (gestational age: 32 weeks, 6 days) and a preeclamptic (gestational age: 28 weeks, 3 days) participant. The participants were in a semirecumbent position with the UPatch placed on the maternal abdomen to monitor the blood flow continuously at the placental cord insertion (Fig. 4a and Supplementary Discussion 20). We derived the fetal heart rate and Doppler indices, including pulsatility index, resistance index and systolic-to-diastolic ratio, which are independent of the ultrasound incident angle (Supplementary Discussion 21)[19]. Both participants showed similar fetal heart rate patterns (Fig. 4b–d). The average fetal heart rates were 149.5 bpm for the healthy and 143.3 bpm for the preeclamptic participant, with variabilities of 20.3 and 21.5 bpm, respectively (Fig. 4b and Supplementary Discussion 22). The UPatch could detect transient fetal heart rate accelerations, which indicate a healthy fetal state (Fig. 4c and Supplementary Fig. 36)[61]. However, the Doppler indices of the participants showed distinct features. There was minimal variability in the Doppler indices of the healthy participant, indicating stable blood flow. The mean pulsatility index of 1.04, resistance index of 0.62 and systolic-to-diastolic ratio of 2.61 aligned with the 50th percentile of established reference norms, indicating a healthy fetus[23]. In contrast, the preeclamptic participant showed large fluctuations in the Doppler indices and the end-diastolic velocity was absent 24.9% of the time (Fig. 4b,d, Supplementary Fig. 37 and Supplementary Discussion 22). The mean pulsatility index of 2.04, resistance index of 0.85 and systolic-to-diastolic ratio of 5.11 were above the 97.5th percentile, suggesting severe placental dysfunction[23]. Following the detection of compromised fetal health using the UPatch, the preeclamptic participant underwent intensive monitoring and the baby was delivered by Cesarean section 4 days later.

Current obstetric practice relies on a two-step process of cardiotocography for fetal heart rate and separate manual Doppler ultrasound for Doppler indices (Supplementary Discussion 23)[56]. We used the UPatch to continuously monitor both signals simultaneously in 52 pregnancies (Supplementary Figs. 36–91 and Supplementary Discussion 24). Cohort analysis showed that the fetal heart rate and Doppler indices were not correlated, highlighting their potential to provide complementary clinical insights (Fig. 4e and Supplementary Fig. 92). Additionally, continuous monitoring results revealed that transient physiological fluctuations can temporarily alter Doppler indices to abnormal values (Supplementary Figs. 36–91). With conventional ultrasound devices, these transient fluctuations may be misinterpreted as pathological and trigger unnecessary interventions, whereas continuous monitoring with the UPatch establishes a personalized baseline and temporal context to distinguish transient fluctuations from sustained compromise. While fetal heart rate decelerations were observed, the substantial beat-to-beat variability and absence of a well-defined gestational reference trend made interpretation challenging (Fig. 4f and Supplementary Fig. 93)[62]. In contrast, Doppler indices exhibited monotonic relationships with gestational age, consistent with established reference ranges[23], supporting their use as objective, clinically actionable information for assessing fetal vascular resistance and identifying high-risk pregnancies (Fig. 4g and Supplementary Figs. 93 and 94). The data were also stratified by perinatal conditions, including healthy, small for gestational age, large for gestational age, gestational diabetes, preeclampsia and gestational hypertension. Fetal heart rate distributions overlapped substantially among all conditions, showing minimal discrimination (Fig. 4h). In contrast, Doppler indices differed, particularly for small for gestational age, preeclampsia and hypertension, illustrating the UPatch's potential to identify high-risk pregnancies in real time (Fig. 4i, Supplementary Figs. 95 and 96 and Supplementary Discussion 25).

Fig. 4 | Continuous monitoring of pregnant participants. a, Photograph of the measurement setup, with a participant in a semirecumbent position. The UPatch was laminated on the maternal abdomen and connected to an ultrasound beam former and a host computer, which displays the duplex image, tracks the sample gate and measures spectral Doppler signals from the umbilical artery. **b**, Histograms of the fetal heart rate (FHR; left), pulsatility index (middle) and resistance index (right) from the healthy (gray) and preeclamptic (red) participants. **c**, Pulsatility index, resistance index (top) and FHR (middle) recordings from the healthy participant, with highlighted spectral Doppler signals from the shaded regions (bottom). The recorded traces share the same scale bar. The spectra share the same scale bar. **d**, Pulsatility index, resistance index (top) and FHR (middle) recordings from the preeclamptic participant, with highlighted spectral Doppler signals from the shaded regions (bottom). The recorded traces share the same scale bar. The spectra share the same scale bar. **e**, Scatter plot of pulsatility index against FHR with each color in the data points corresponding to an individual participant. Participant 1 corresponds to the healthy participant and participant 2 corresponds to the preeclamptic participant in **b**–**d**. The corresponding color scheme for all participants is provided in Supplementary Figs. 88–91. **f**, FHR plotted against gestational age ($n = 241$). **g**, Pulsatility index plotted against gestational age ($n = 241$). The black dashed line is the 50th percentile and the solid black lines are the 5th and 95th percentiles of a widely used reference population[23]. Data in **f**,**g** are presented as the mean ± s.d. **h**,**i**, Box plots of FHR (**h**) and pulsatility index (**i**) stratified by perinatal conditions: healthy (31 participants, 217 data points), small for gestational age (SGA; seven participants, 49 data points), large for gestational age (LGA; three participants, 21 data points), diabetes (DB; six participants, 42 data points), preeclampsia (PE; seven participants, 49 data points) and maternal hypertension (HYN; ten participants, 70 data points). Each box represents the interquartile range (25th–75th percentiles), the whiskers denote the 5th–95th percentile range and the midline indicates the median. Each participant's data were segmented into 10-min intervals ($n = 7$ per participant). The color schemes in **e**–**i** are the same.

https://doi.org/10.1038/s41587-026-03140-1

Discussion

The UPatch can visualize fetal anatomy and measure fetal heart rate and blood flow, offering complementary insights to existing approaches to evaluate fetal health. Whereas standard clinical regimens mandate periodic blood flow assessments performed by sonographers, typically at weekly intervals in outpatient settings and up to three times per week for inpatients, these evaluations are labor intensive and prone to errors[57]. In contrast, the UPatch adheres directly to the maternal abdomen for hands-free use and implements an image segmentation-based algorithm to identify and track blood vessels autonomously, enabling continuous and accurate blood flow measurements without the need for a sonographer.

Several strategies could be pursued to improve the UPatch further. First, the tracking algorithm cannot maintain uninterrupted spectral Doppler waveforms during motion because vessel tracking and spectral Doppler acquisition occur sequentially. This limitation can be solved by integrating a separate image segmentation algorithm to detect signal loss in real time, allowing the system to pause the spectral Doppler

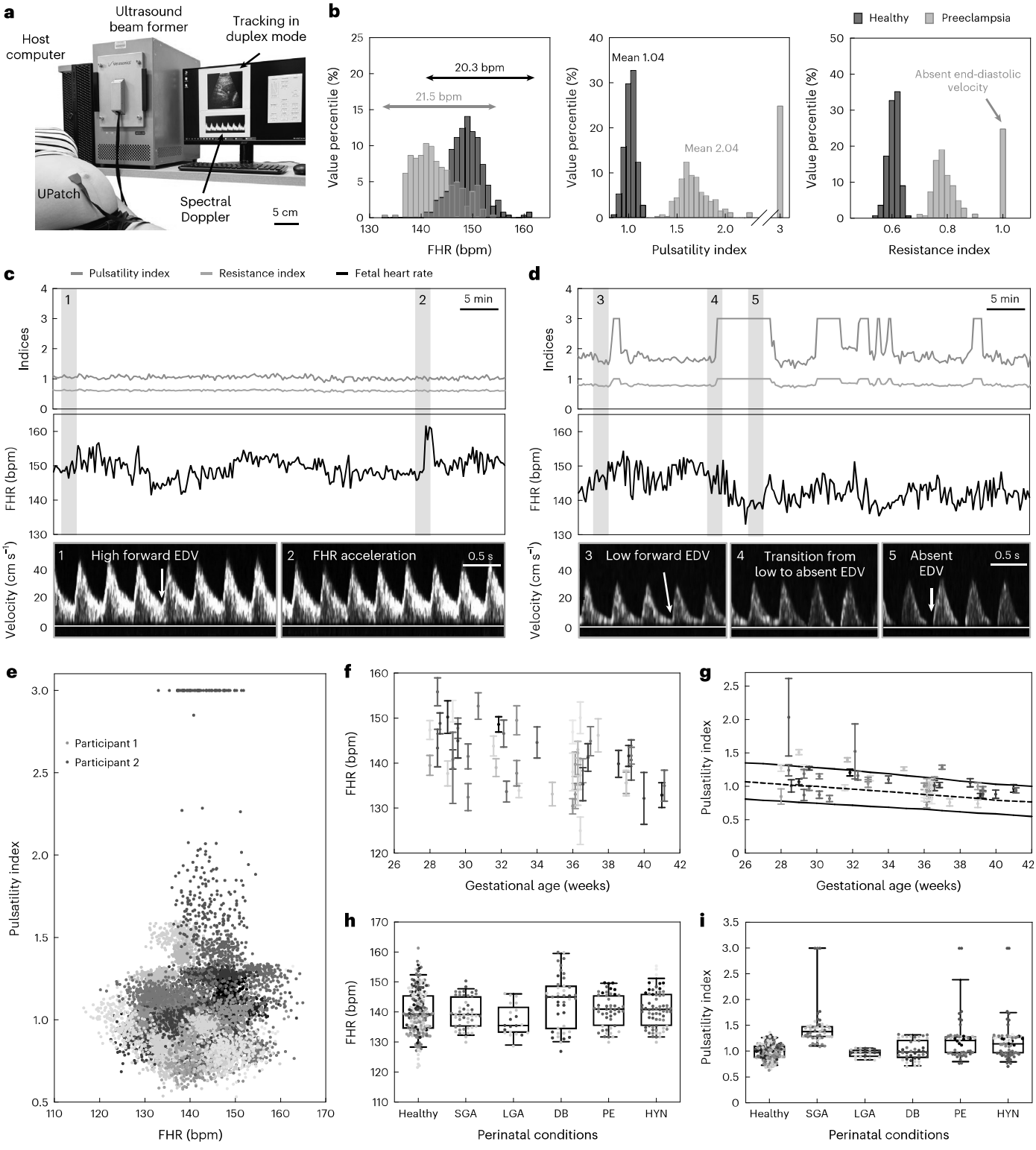

sequence and track the target vessel in the duplex image. Leveraging advanced graphics processing units would substantially accelerate computation, enabling simultaneous duplex imaging and spectral Doppler acquisition (Supplementary Discussion 17)[63,64].

Second, the UPatch currently needs to be wired to a bulky back-end system for both power and high-bandwidth data transmission, like many other wearable devices[28,31,65–69]. While this configuration is appropriate for inpatient settings, it limits mobility and broader applicability. Future developments could incorporate wireless circuits to expand the range of clinical scenarios. A compact circuit was recently developed to interface a transducer array with a single transceiver for vessel pulsation monitoring but it is not capable of Doppler imaging (Supplementary Discussion 26)[70]. Developing a more advanced circuit with multiple transceivers for Doppler imaging would enhance user mobility, help assess the impact of maternal posture and physical activity on fetal health and show how maternal circulation affects fetal hemodynamics[71].

Third, this study was limited to using only the UPatch. Future work could focus on integrating UPatch data streams (such as fetal heart rate and Doppler indices) with additional physiological metrics from both the fetus (such as electrocardiography) and the mother (such as blood pressure, pulse oximetry and tocodynamometry). Such multimodal integration would provide a more comprehensive and accurate understanding of the dynamic interactions between fetus and mother[11].

Lastly, applying big data analysis to correlate UPatch data streams with postnatal and postmortem results would yield unprecedented insights into the mechanisms of fetal complications, advancing diagnosis and intervention strategies[72].

Online content

Any methods, additional references, Nature Portfolio reporting summaries, source data, extended data, supplementary information, acknowledgements, peer review information; details of author contributions and competing interests; and statements of data and code availability are available at https://doi.org/10.1038/s41587-026-03140-1.

References

1. Woodward, P. J., Kennedy, A. & Sohaey, R. *Diagnostic Imaging: Obstetrics* 4th edn (Elsevier, 2021).
2. Hutter, D., Kingdom, J. & Jaeggi, E. Causes and mechanisms of intrauterine hypoxia and its impact on the fetal cardiovascular system: a review. *Int. J. Pediatr.* **2010**, 401323 (2010).
3. Berkley, E., Chauhan, S. P. & Abuhamad, A. Doppler assessment of the fetus with intrauterine growth restriction. *Am. J. Obstet. Gynecol.* **206**, 300–308 (2012).
4. Nelson, K. B. & Grether, J. K. Causes of cerebral palsy. *Curr. Opin. Pediatr.* **11**, 487–491 (1999).
5. McClure, E. et al. Global Network for Women's and Children's Health Research: probable causes of stillbirth in low- and middle-income countries using a prospectively defined classification system. *BJOG* **125**, 131–138 (2018).
6. Smith, G. C. S. & Fretts, R. C. Stillbirth. *Lancet* **370**, 1715–1725 (2007).
7. Lawn, J. E. et al. Stillbirths: rates, risk factors, and acceleration towards 2030. *Lancet* **387**, 587–603 (2016).
8. Rouse, D. J. Antepartum fetal surveillance ACOG practice bulletin, number 229. *Obstet. Gynecol.* **137**, E116–E127 (2021).
9. Rouse, D. J., Owen, J., Goldenberg, R. L. & Cliver, S. P. Determinants of the optimal time in gestation to initiate antenatal fetal testing: a decision-analytic approach. *Am. J. Obstet. Gynecol.* **173**, 1357–1363 (1995).
10. Harkey, K. T., Casale, M. B., Pantelopoulos, A. A. & Zurcher, M. A. Assessing the clinical use of a novel, mobile fetal monitoring device. *Obstet. Gynecol.* **123**, 55S (2014).
11. Ryu, D. et al. Comprehensive pregnancy monitoring with a network of wireless, soft, and flexible sensors in high- and low-resource health settings. *Proc. Natl Acad. Sci. USA* **118**, e2100466118 (2021).
12. Freeman, R. K. Problems with intrapartum fetal heart rate monitoring interpretation and patient management. *Obstet. Gynecol.* **100**, 813–826 (2002).
13. Grivell, R. M., Alfirevic, Z., Gyte, G. M. & Devane, D. Antenatal cardiotocography for fetal assessment. *Cochrane Database Syst. Rev.* **9**, CD007863 (2015).
14. Alfirevic, Z., Devane, D., Gyte, G. M. & Cuthbert, A. Continuous cardiotocography (CTG) as a form of electronic fetal monitoring (EFM) for fetal assessment during labour. *Cochrane Database Syst. Rev.* **2**, CD006066 (2017).
15. Marzbanrad, F., Stroux, L. & Clifford, G. D. Cardiotocography and beyond: a review of one-dimensional Doppler ultrasound application in fetal monitoring. *Physiol. Meas.* **39**, 08TR01 (2018).
16. Hayes-Gill, B. R. Monica Healthcare: from the research laboratory to commercial reality—a real-life case study. *Healthc. Technol. Lett.* **8**, 1–10 (2021).
17. Gunther, J. E., Jayet, B., Sekar, S. K. V., Kainerstorfer, J. M. & Andersson-Engels, S. Review of optical methods for fetal monitoring in utero. *J. Biophotonics* **15**, e202100343 (2022).
18. Du, Y.-C., Yen, L. B., Kuo, P.-L. & Tsai, P.-Y. A wearable device for evaluation of relative position, force, and duration of fetal movement for pregnant woman care. *IEEE Sens. J.* **21**, 19341–19350 (2021).
19. Nicolaides, K., Rizzo, G., Hecher, K. & Ximenes, R. *Doppler in Obstetrics* (The Fetal Medicine Foundation, 2002).
20. Salomon, L. J. et al. ISUOG Practice Guidelines: ultrasound assessment of fetal biometry and growth. *Ultrasound Obstet. Gynecol.* **53**, 715–723 (2019).
21. Bhide, A. et al. ISUOG Practice Guidelines (updated): use of Doppler velocimetry in obstetrics. *Ultrasound Obstet. Gynecol.* **58**, 331–339 (2021).
22. Oros, D. et al. Reference ranges for Doppler indices of umbilical and fetal middle cerebral arteries and cerebroplacental ratio: systematic review. *Ultrasound Obstet. Gynecol.* **53**, 454–464 (2019).
23. Drukker, L. et al. International gestational age-specific centiles for umbilical artery Doppler indices: a longitudinal prospective cohort study of the INTERGROWTH-21st Project. *Am. J. Obstet. Gynecol.* **222**, 602.e1–602.e15 (2020).
24. Kiserud, T. et al. The World Health Organization fetal growth charts: a multinational longitudinal study of ultrasound biometric measurements and estimated fetal weight. *PLOS Med.* **14**, e1002220 (2017).
25. Papageorghiou, A. T. et al. International standards for fetal growth based on serial ultrasound measurements: the fetal growth longitudinal study of the INTERGROWTH-21st Project. *Lancet* **384**, 869–879 (2014).
26. Goldenberg, R. L., Harrison, M. S. & McClure, E. M. Stillbirths: the hidden birth asphyxia—US and global perspectives. *Clin. Perinatol.* **43**, 439–453 (2016).
27. AIUM practice parameter for the performance of standard diagnostic obstetric ultrasound. *J. Ultrasound Med.* **43**, E20–E32 (2024).
28. Wang, C. et al. Bioadhesive ultrasound for long-term continuous imaging of diverse organs. *Science* **377**, 517–523 (2022).
29. Hu, H. et al. A wearable cardiac ultrasound imager. *Nature* **613**, 667–675 (2023).
30. Du, W. et al. Conformable ultrasound breast patch for deep tissue scanning and imaging. *Sci. Adv.* **9**, eadh5325 (2023).
31. Zhang, L. et al. A conformable phased-array ultrasound patch for bladder volume monitoring. *Nat. Electron.* **7**, 77–90 (2023).

32. Khalil, A. et al. ISUOG Practice Guidelines: performance of third-trimester obstetric ultrasound scan. *Ultrasound Obstet. Gynecol.* **63**, 131–147 (2024).
33. Hoskins, P. R., Martin, K. & Thrush, A. (eds) *Diagnostic Ultrasound Physics and Equipment* (CRC Press, 2019).
34. Evans, D. H., Jensen, J. A. & Nielsen, M. B. Ultrasonic colour Doppler imaging. *Interface Focus* **1**, 490–502 (2011).
35. Zhang, L., Du, W., Kim, J.-H., Yu, C.-C. & Dagdeviren, C. An emerging era: conformable ultrasound electronics. *Adv. Mater.* **36**, e2307664 (2024).
36. Aksoy, B. et al. Shielded soft force sensors. *Nat. Commun.* **13**, 4649 (2022).
37. Institute of Physics and Engineering in Medicine. *IPEM Report 102—Quality Assurance of Ultrasound Imaging Systems*. (IPEM, 2010).
38. Thijssen, J. M., van Wijk, M. C. & Cuypers, M. H. M. Performance testing of medical echo/Doppler equipment. *Eur. J. Ultrasound* **15**, 151–164 (2002).
39. Browne, J. E. A review of Doppler ultrasound quality assurance protocols and test devices. *Physica Medica* **30**, 742–751 (2014).
40. Ter Haar, G. (ed.) *The Safe Use of Ultrasound in Medical Diagnosis* (The British Institute of Radiology, 2012).
41. AIUM official statement for recommended maximum scanning times for displayed thermal index values. *J. Ultrasound Med.* **42**, E74–E75 (2023).
42. Safety Group of the British Medical Ultrasound Society. *Guidelines for the Safe Use of Diagnostic Ultrasound Equipment*. (BMUS, 2010).
43. Food and Drug Administration. *Marketing Clearance of Diagnostic Ultrasound Systems and Transducers: Guidance for Industry and Food and Drug Administration Staff*. Report No. FDA-2017-D-5372 (FDA, 2023).
44. Hekkenberg, R. T. & Bezemer, R. A. *Aspects Concerning the Measurement of Surface Temperature of Ultrasonic Diagnostic Transducers, Part 2: On a Human and Artificial Tissue*. (TNO Preventie en Gezondheid, 2003).
45. International Electrotechnical Commission. *Ultrasonics: Field Characterization—Test Methods for the Determination of Thermal and Mechanical Indices Related to Medical Diagnostic Ultrasonic Fields*. Report No. IEC 62359:2010/AMD1:2017 (IEC, 2017).
46. Maulik, D. & Lees, C. C. (eds) *Doppler Ultrasound in Obstetrics and Gynecology* (Springer, 2023).
47. Conde-Agudelo, A., Villar, J., Kennedy, S. H. & Papageorghiou, A. T. Predictive accuracy of cerebroplacental ratio for adverse perinatal and neurodevelopmental outcomes in suspected fetal growth restriction: systematic review and meta-analysis. *Ultrasound Obstet. Gynecol.* **52**, 430–441 (2018).
48. Hadlock, F. P., Harrist, R. B., Sharman, R. S., Deter, R. L. & Park, S. K. Estimation of fetal weight with the use of head, body, and femur measurements—a prospective study. *Am. J. Obstet. Gynecol.* **151**, 333–337 (1985).
49. Zhou, S. et al. Transcranial volumetric imaging using a conformal ultrasound patch. *Nature* **629**, 810–818 (2024).
50. Oates, C. *Ultrasound Technology for Clinical Practitioners* (Wiley, 2023).
51. Ali, S. et al. Prognostic accuracy of antenatal Doppler ultrasound for adverse perinatal outcomes in low-income and middle-income countries: a systematic review. *BMJ Open* **11**, e049799 (2021).
52. Ali, S. et al. Standardization and quality control of Doppler and fetal biometric ultrasound measurements in low-income setting. *Ultrasound Obstet. Gynecol.* **61**, 481–487 (2023).
53. Demi, L. Practical guide to ultrasound beam forming: beam pattern and image reconstruction analysis. *Appl. Sci.* **8**, 1544 (2018).
54. Ronneberger, O., Fischer, P. & Brox, T. U-Net: convolutional networks for biomedical image segmentation. In *Proceedings of the Medical Image Computing and Computer-Assisted Intervention* (eds Navab, N., Hornegger, J., Wells, W. M. & Frangi, A. F.) (Springer, 2015).
55. Shi, X. et al. Convolutional LSTM network: a machine learning approach for precipitation nowcasting. In Proceedings of the 29th International Conference on Neural Information Processing Systems (eds Cortes, C., Lee, D. D., Sugiyama, M. & Garnett, R.) (ACM, 2015).
56. Alfirevic, Z., Stampalija, T. & Dowswell, T. Fetal and umbilical Doppler ultrasound in high-risk pregnancies. *Cochrane Database Syst. Rev.* **6**, CD007529 (2017).
57. Lees, C. C. et al. ISUOG Practice Guidelines: diagnosis and management of small-for-gestational-age fetus and fetal growth restriction. *Ultrasound Obstet. Gynecol.* **56**, 298–312 (2020).
58. Sotiriadis, A. et al. ISUOG Practice Guidelines: role of ultrasound in screening for and follow-up of pre-eclampsia. *Ultrasound Obstet. Gynecol.* **53**, 7–22 (2019).
59. Vogel, J. P. et al. The global epidemiology of preterm birth. *Best Pract. Res. Clin. Obstet. Gynaecol.* **52**, 3–12 (2018).
60. Gardosi, J., Madurasinghe, V., Williams, M., Malik, A. & Francis, A. Maternal and fetal risk factors for stillbirth: population based study. *BMJ* **346**, f108 (2013).
61. Freeman, R. K., Garite, T. J., Nageotte, M. P. & Miller, L. A. *Fetal Heart Rate Monitoring* 4th edn (Lippincott Williams & Wilkins, 2012).
62. Pildner Von Steinburg, S. et al. What is the 'normal' fetal heart rate? *PeerJ* **1**, e82 (2013).
63. Chang, L. W., Hsu, K. H. & Li, P. C. Graphics processing unit-based high-frame-rate color doppler ultrasound processing. *IEEE Trans. Ultrason. Ferroelectr. Freq. Control* **56**, 1856–1860 (2009).
64. So, H., Chen, J., Yiu, B. & Yu, A. Medical ultrasound imaging: to GPU or not to GPU? *IEEE Micro* **31**, 54–65 (2011).
65. Lee, W. et al. Universal assembly of liquid metal particles in polymers enables elastic printed circuit board. *Science* **378**, 637–641 (2022).
66. You, I. et al. Artificial multimodal receptors based on ion relaxation dynamics. *Science* **370**, 961–965 (2020).
67. Wang, S. et al. Skin electronics from scalable fabrication of an intrinsically stretchable transistor array. *Nature* **555**, 83–88 (2018).
68. Son, D. et al. Multifunctional wearable devices for diagnosis and therapy of movement disorders. *Nat. Nanotechnol.* **9**, 397–404 (2014).
69. Liu, Z. et al. A three-dimensionally architected electronic skin mimicking human mechanosensation. *Science* **384**, 987–994 (2024).
70. Lin, M. et al. A fully integrated wearable ultrasound system to monitor deep tissues in moving subjects. *Nat. Biotechnol.* **42**, 448–457 (2024).
71. Skow, R. J. et al. Effects of prenatal exercise on fetal heart rate, umbilical and uterine blood flow: a systematic review and meta-analysis. *Br. J. Sports Med.* **53**, 124–133 (2019).
72. Georgieva, A., Abry, P., Nunes, I. & Frasch, M. G. Editorial: Fetal–maternal monitoring in the age of artificial intelligence and computer-aided decision support: a multidisciplinary perspective. *Front. Pediatr.* **10**, 2296–2360 (2022).

[1]Aiiso Yufeng Li Family Department of Chemical and Nano Engineering, University of California, San Diego, La Jolla, CA, USA. [2]Department of Anesthesiology, Perioperative and Pain Medicine, Stanford University, Stanford, CA, USA. [3]Materials Science and Engineering Program, University of California, San Diego, La Jolla, CA, USA. [4]Department of Electrical and Computer Engineering, University of California, San Diego, La Jolla, CA, USA. [5]Shu Chien–Gene Lay Department of Bioengineering, University of California, San Diego, La Jolla, CA, USA. [6]Nuffield Department of Women's and Reproductive Health, University of Oxford, Oxford, UK. [7]Department of Computer Science and Engineering, University of California, San Diego, La Jolla, CA, USA. [8]Qualcomm Institute Makerspace, University of California, San Diego, La Jolla, CA, USA. [9]Department of Obstetrics, Gynecology, and Reproductive Sciences, University of California, San Diego, La Jolla, CA, USA. [10]Independent Researcher, Rockville, MD, USA. [11]Department of Radiology, University of California, San Diego, La Jolla, CA, USA. [12]These authors contributed equally: Geonho Park, Yizhou Bian, Hao Huang, Sai Zhou. ✉e-mail: antoniya.georgieva@wrh.ox.ac.uk; shengxu@stanford.edu

Methods

Fabrication of the UPatch

The fabrication process can be divided into three steps: (1) transducer assembly; (2) electrode printing and acoustic lens integration; and (3) device packaging.

Transducer assembly. A silicone (Ecoflex-0030, Smooth-On) layer was first spin-coated at 3,000 rpm for 60 s on two glass slides and cured in an 80 °C oven as temporary substrates. Conductive epoxy (Von Roll 3022 E-Solder, EIS) was prepared as the backing layer by mixing an Ag–epoxy composite with a hardener in a 12.5:1 weight ratio and subsequently degassed in a vacuum desiccator. Then, a 1–3 composite was placed on the silicone surface of one glass slide. The degassed conductive epoxy was placed on top and covered by the other silicone-coated glass slide, followed by curing at room temperature for 24 h. The thickness of the backing layer (400 µm in this study) was controlled by placing certain spacers in between the two glass slides.

After curing, the glass slides were removed, and the transducer made of 1–3 composite and backing was diced. To ensure direct transfer of the backing layer side of the transducer to the signal electrodes, the 1–3 composite side of the transducer was first placed on an ultraviolet tape (UHP-110M3, Denka) with a frame film applicator (UH114, Ultron Systems). Then, the transducer was diced with a dicing machine (DAD3221, Disco) to 25.55 mm by 12 mm using a diamond blade (ZH14-SD1700-V1-90 GE, Disco) at 25,000 rpm for the spindle and 0.5 mm s^{-1} feed speed. A second diamond blade (Z09-SD4000-Y1-60, Disco) was used to dice the 0.05-mm kerf of the transducer. Super multipass dicing was performed with 50-µm (depth) stepwise cuts at 40,000 rpm for the spindle and 10 mm s^{-1} feed speed to minimize blade and transducer vibration during dicing (Supplementary Fig. 2 and Supplementary Discussion 7). Lastly, the diced transducers were detached from the ultraviolet tape using an ultraviolet curing system (UH104, Ultron Systems).

Electrode printing and acoustic lens integration. The substrate for electrode printing was prepared by spin-coating polydimethylsiloxane (Sylgard 184) at 3,000 rpm for 60 s on a glass slide, followed by curing in an 80 °C oven as a temporary substrate. Then, polyimide and copper laminates (AC181200EN, DuPont) and the polydimethylsiloxane-coated glass slide were activated by ultraviolet light (PSD series Digital UV Ozone System, Novascan) and bonded together. Electrode patterns (such as electromagnetic shielding, mesh ground electrode and two signal electrodes) designed with AutoCAD (Autodesk) were laser ablated (G4 pulsed fiber laser, wavelength: 1,095–1,065 nm, energy: 0.228 mJ, frequency: 35 kHz, speed: 300 mm s^{-1}, and pulse width: 500 ns) on the polyimide and copper laminate (Supplementary Fig. 9). Two polyimide masks were prepared by laser ablation for dispensing conductive epoxy on the transducer bonding pads of the two signal electrode layers.

For acoustic lens integration, an aluminum mold was designed with Solidworks (Dassault Systemes) and machined using a computer with numerically controlled machining (Tormach 1100MX, Tormach) at a spindle speed of 10,000 rpm and feed rate of 40 inches per min (Supplementary Fig. 6 and Supplementary Discussion 8). The mold was cleaned with isopropanol before silicon elastomer was cured in the mold and used as the acoustic lens.

Device packaging. First, polyimide tapes were adhered to two glass slides to ensure device detachment after final packaging. Silicone (Ecoflex-0030, Smooth-On) mixed with black dye was spin-coated on the polyimide tape at 4,000 rpm for 60 s, followed by curing at room temperature for 2 h. The electromagnetic shielding layer, which was transferred onto a water-soluble tape (AQUASOL), and the silicone-coated glass slide were activated by ultraviolet light and bonded together, followed by heating in an 80 °C oven for 30 min. After the water-soluble tape was dissolved, a silicone layer was spin-coated on top at 4,000 rpm for 60 s, followed by curing.

Similarly, the first layer of the signal electrode was aligned and transferred onto the electromagnetic shielding layer using a water-soluble tape. A polyimide mask was placed on the signal electrode to protect the transducer bonding pads of the electrode from another silicone layer spin-coated on top. After the polyimide mask was removed and the silicone layer was cured, the second layer of the signal electrode was aligned and stacked onto the first layer of the signal electrode. Conductive epoxy was dispensed onto the transducer bonding pads of both signal electrodes through a polyimide mask. After the mask was removed, the backing layer side of the diced transducers was aligned and bonded by curing the conductive epoxy for 8 h at room temperature and then 2 h at 40 °C. Flexible printed circuit cables were bonded to the signal electrodes using solder paste ($Sn_{42}Bi_{57.6}Ag_{0.4}$, melting point: 138 °C).

The mesh ground electrode was bonded to a silicone-coated glass slide. After conductive epoxy was dispensed using a polyimide mask, the mesh ground electrode was aligned and cured onto the transducers. The exterior boundaries of the mesh ground electrode and electromagnetic shielding layer were connected with vertical interconnect accesses by soldering copper wires (Remington Industries) to create a Faraday cage (Supplementary Fig. 10 and Supplementary Discussion 9)[73]. After the device was fully encapsulated with silicone elastomer, the glass slides were removed. Lastly, the acoustic lens was aligned and bonded with silicone elastomer onto the packaged transducers.

Quality assurance

The UPatch was transmitted at a frequency of 2.5 MHz with a sampling rate of 10 MHz. Apodization was uniform across 64 channels with the imaging view angle of 45°. The number of compounding angles was 21 with a step size of 0.75° for brightness mode imaging. The ensemble length was 14 for color-flow mode. Doppler modes used a pulse repetition frequency of 3,000 Hz. The sample gate size for spectral Doppler was 2 mm.

The UPatch was characterized using two phantom setups and compared to a handheld clinical ultrasound device (P4-1, ATL), both transmitting at 2.5 MHz. Both the UPatch and the clinical device were connected to the Vantage 256 (Verasonics), rather than connecting the P4-1 device to a clinical backend system (Voluson E10, GE Healthcare). This method allows comparison of the probe performance more fairly and avoids confounding effects from differences in backend signal processing.

First, the brightness mode was characterized with a multipurpose phantom (ATS 539, CIRS) (Supplementary Fig. 15)[37,38]. Monofilament wires were used to determine the axial and lateral resolutions. A volume of water on top of the phantom was used as a standoff to characterize depths up to 20 cm. The distance between two adjacent pixels in the axial and lateral directions was calculated as follows:

$$\Delta y = \frac{\text{depth}}{N_{\text{pixel, axial}} - 1} \quad (1)$$

$$\Delta x = \frac{\text{depth}}{N_{\text{pixel, lateral}} - 1} \quad (2)$$

The full width at half maximum of the point spread function for each wire in the axial and lateral directions was measured. The axial and lateral resolutions were calculated by multiplying the number of pixels within the full width at half maximum and adjacent pixel distance. The six tissue-mimicking contrast targets in the phantom were used to characterize the dynamic range and contrast-to-noise ratio[38]. The dynamic range was calculated by linearly fitting among the six grayscale targets and finding the maximum positive and negative

contrasts corresponding to gray values of 255 and 0. Then, the negative one was subtracted from the other. The contrast-to-noise ratio was calculated as follows:

$$\text{Contrast}-\text{to}-\text{noise ratio} = \frac{|\mu_{\text{in}} - \mu_{\text{out}}|}{\sqrt{\sigma_{\text{in}}^2 + \sigma_{\text{out}}^2}} \quad (3)$$

where μ_{in} and σ_{in} are the mean and s.d. of pixel intensities within each target and μ_{out} and σ_{out} are the mean and s.d. of pixel intensities outside each target. The contrast and contrast-to-noise ratio were computed on the basis of displayed images rather than raw radiofrequency signals or in-phase and quadrature data, meaning that the values were derived from log-compressed images[74].

The color and spectral Doppler modes were characterized with Doppler fluid (769DF, CIRS) pumped into a Doppler phantom (ATS 523A, CIRS) with diameters of 2, 4, 6 and 8 mm using a peristaltic pump (Supplementary Fig. 16)[39]. The UPatch was positioned at varying distances from 30 mm to 120 mm at intervals of 10 mm from the phantom. The signal-to-noise ratio in the color-flow images was calculated by increasing the color gain to maximum to obtain a noise level in the tissue-mimicking phantom. The accuracy of spectral Doppler was measured by comparison to a known velocity from the peristaltic pump at different depths and velocities.

Acoustic exposure and thermal measurement protocols

Hydrophone. A needle hydrophone (HNP-0400, ONDA) was connected to a right-angle adapter (ONDA), preamplifier (AH-2010-100, ONDA) and DC block (BNP, ONDA) and suspended in deionized water (Supplementary Fig. 23) (https://www.ondacorp.com/Handbook/). The signals were read with an oscilloscope (PicoScope 5000 Series, Pico Technology). At 2.5 MHz, the effective sensitive element diameter (a more meaningful measure of spatial resolution than the geometrical sensitive element diameter, which was 400 µm) was estimated to be 480 µm (ref. 75). The uncertainties of hydrophone-based pressure, intensity and power measurements were ~15% (ref. 76).

The hydrophone system was calibrated <1 year before the measurement. The calibration $M_c(f)$ is the hydrophone end-of-cable open circuit sensitivity, which can be converted as follows:

$$M_C(f) = 10^{\frac{M_C(f)_{\text{dB rel.}}+120}{20}} \quad (4)$$

where $M_C(f)$ is the sensitivity in V per Pa and $M_C(f)_{\text{dB rel.}}$ is the sensitivity in decibels relative to 1 V per µPa (https://www.ondacorp.com/Handbook/). The manufacturer's sensitivity magnitude data (that is, relative calibration from 1 to 20 MHz) was used to perform magnitude-based waveform deconvolution to compensate for the hydrophone's nonuniform frequency response in the signal spectrum (Supplementary Fig. 23). Magnitude-based deconvolution has been shown to be nearly as effective as complex deconvolution for improving the accuracy of pressure and intensity measurements[77]. Additionally, because the ratio of the hydrophone sensitive element diameter d_g to the product of the wavelength λ and $F/\#$ (ratio of focal distance to aperture width) $\ll 1$, a hydrophone spatial averaging correction was not necessary[78].

Considering the capacitive load of the preamplifier when converting the voltage measurements to pressure values, the loaded sensitivity $M_L(f)$ can be estimated as follows:

$$M_L(f) = G(f)\,M_C(f)\,\frac{C_H}{C_H + C_A + C_c} \quad (5)$$

where $G(f)$ is the preamplifier gain (20 dB in this study), C_{H} is the capacitance of the hydrophone (70 pF in this study), C_{A} is the capacitance of the preamplifier (7 pF in this study), and C_{C} is the capacitance of the right-angle adapter (1.6 pF in this study) (https://www.ondacorp.com/Handbook/).

A hydrophone controlled by a three-dimensional linear motor in a water tank was used to measure the acoustic signal intensity (Supplementary Fig. 23). Transverse scans with scanning increments of Δx = 0.5 mm (approximately one effective hydrophone diameter) and Δy = 0.5 mm and an axial scan with scanning increments of Δz = 0.5 mm from breakpoint depth to focal depth were performed (Supplementary Discussion 11)[79]. Two different beam-forming methods were measured separately: diverging beam (for brightness and color-flow mode) and focused beam (for spectral Doppler mode) that was focused at every 1 cm (depth; between 5 and 15 cm) along the beam axis. The UPatch was activated at 30 V with a pulse repetition frequency of 3,000 Hz. Power was derived from the hydrophone scan data by integrating over a transverse plane within the beam cross-sectional area where the intensity was at least −26.2 dB of the peak value. All measurements were calculated on the basis of the settings used for duplex imaging and spectral Doppler because these were the modes used during continuous monitoring in this study.

Radiation force balance. Power measurements were obtained from a radiation force balance (RFB-2000, ONDA) with a flat absorbing target, which could accurately measure power levels up to 2 W (Supplementary Fig. 24) (https://www.ondacorp.com/radiation-force/#:~:text=Designed%20specifically%20for%20easy%20Ultrasound,and%20with%20associated%20IEC%20standards). First, a 1-g weight was used to calibrate the radiation force balance. The calibration constant obtained was 0.9699 A N^{-1}, which fell in the range designed by ONDA (0.9–1.1 A N^{-1}). The distance between the radiation force balance and the UPatch was set to ≥1 cm to avoid thermal and electrical coupling effects between the radiation force balance and the UPatch. Acoustic output power was obtained from the entire aperture of the UPatch and the bounded-square output power over a 1-cm^2 area was measured by masking the UPatch.

The thermal index was calculated on the basis of acoustic output power measurements from both the radiation force balance and hydrophone scan in the transverse plane, providing two independent measurements to minimize uncertainty in the calculation[45].

Surface temperature testing. The surface temperature of the UPatch was evaluated under two scenarios to simulate clinical conditions based on IEC 60601-2-37 (ref. 80). Although the standard requires only 30-min testing[80], we extended the assessments to 48 h to ensure compliance with regulatory standards even under prolonged operation.

First, a phantom test was performed to replicate the setup in the hospital (Supplementary Fig. 22). The phantom consisted of a silicone-based skin (NPL) and agar-based tissue (NPL) with acoustic and thermal properties similar to those of human skin and tissue, respectively. A type K thermocouple (5SRTC-TT-KI-40-1M, OMEGA) with a thickness of 75 µm (ultrasound wavelength at 2.5 MHz) was placed on top of the skin mimicking phantom to measure the surface temperature of the UPatch[44].

Second, to evaluate thermal changes when the UPatch was activated in air, surface temperature was measured. Because the UPatch–air interface has a higher acoustic impedance mismatch compared to that of the UPatch–tissue phantom interface, more heat is expected to be generated in the air[44]. The UPatch was suspended on a clean surface in a stationary position with minimal airflow across the transducer area. The same thermocouple was adhered to the UPatch for temperature measurement.

Evaluation of the vessel-tracking algorithm

The comparative analysis of the lateral and axial discrepancies in defining the sample gates between the tracking algorithm and a sonographer was performed using a double-blind method (Supplementary Discussion 18). The tracking algorithm and the sonographer each selected sample gates independently from 1,000 duplex images,

without access to the other's chosen locations. This design was used to prevent bias in sample gate placement and to ensure an objective comparison between algorithm-selected and sonographer-selected measurements, with discrepancies quantified by the spatial distance between the selected gates. The lateral and axial discrepancies were calculated between the two sample gates (Fig. 3d). A 2-mm sample gate length is commonly used in hospitals (Supplementary Discussion 19)[1]. Thus, within a 2-mm discrepancy between the tracking algorithm and the sonographer, the sample gate was considered to acquire spectral Doppler signals accurately.

Additionally, a new dataset was acquired, containing 500 duplex images from scanning the clinical device on a participant and 500 duplex images from the UPatch on another participant. The tracking algorithm identified the sample gates in all 1,000 images. We engaged three experienced sonographers, each with 30, 8 and 20 years of fetal ultrasonography experience, to independently assess the tracking performance on 1,000 images (Extended Data Fig. 7). This validation method aligns with the recently FDA-cleared cardiac Doppler tracking algorithm (https://www.accessdata.fda.gov/cdrh_docs/pdf23/K232145.pdf), which also relied on three sonographers and evaluated only 168 images. All three sonographers evaluated the tracking algorithm with a customized graphical user interface in Matlab R2023b (Mathworks). 'Optimal' was defined by the sonographer as the tracked sample gate that could potentially be used for spectral Doppler acquisition, 'suboptimal' was defined as the sample gate potentially providing low-quality spectral Doppler signals, and 'nondiagnostic' was defined as the sample gate that could not provide any spectral Doppler signal (Extended Data Fig. 7 and Supplementary Discussion 18).

Lastly, the tracking algorithm was evaluated with the UPatch based on the systolic-to-diastolic ratio of a participant (Supplementary Discussion 18). Each pair of measurements was acquired sequentially by a sonographer and the tracking algorithm. For the mean difference ± s.d. between the UPatch and clinical device, it is expected that the device differences and physiological variability increase the spread of values, even when the overall bias remains very small (Fig. 2f). By eliminating interdevice variability and focusing merely on sample gate selection, the tracking algorithm analysis yields a narrower distribution, even though the mean offset is slightly larger (Fig. 3f). Notably, the mean values reflect different reference comparisons and are not expected to be identical, whereas the reduced s.d. reflects the elimination of device-related variability.

Human test protocol

All human tests were approved by the Institutional Review Board of the University of California, San Diego (804817) and the UK Research Ethics Committee (23/WA/0032). The participants all gave voluntary consent to the UPatch tests and all measurements were conducted by a clinician. The study included 62 participants for accuracy validation (Fig. 2f, Table 1 and Supplementary Fig. 30) and 52 participants for continuous monitoring (Supplementary Figs. 36–91). This dataset captures a broad range of clinical conditions across the study cohort, including variations in fetal biometry (for example, small and large for gestational age) (Fig. 4h,i and Supplementary Figs. 95 and 96) and gestational age (Table 1). For the validation test, three pairs of measurements were acquired from the UPatch and a handheld clinical ultrasound device (Voluson E10, GE Healthcare) on 62 participants. For continuous monitoring, the clinical device was used to locate the position of the vessel. Then, the UPatch was taped on the maternal abdomen for continuous monitoring. The measurements were acquired at 15 s intervals. The current study was conducted under inpatient conditions, where pregnant participants were free to move within the limits of standard clinical monitoring. During the recordings, the pregnant participants naturally moved within their beds, accompanied by various fetal behavioral states, fetal movements and uterine contractions.

While healthy pregnancies typically exhibit strong forward end-diastolic flow, severe pathological pregnancies can have reduced, absent or reversed end-diastolic flow, resulting in weaker diastolic spectral content and increased waveform variability[3,81]. In these cases, pulse repetition frequency of Doppler ultrasound becomes particularly critical; if it is too high, low velocity components are compressed near the waveform baseline and become difficult to distinguish from noise, while a pulse repetition frequency that is too low risks aliasing at peak systolic velocities[33]. To ensure a fair and clinically relevant comparison across healthy and severe pathological conditions, validation was performed using matched pulse repetition frequency settings between the UPatch and clinical ultrasound system.

The UPatch was designed for easy repositioning as needed. It is movable, can be sanitized with alcohol wipes and can be repositioned without compromising functionality. This allows adaptability in clinical use while maintaining hygiene and user comfort.

For fetal biometry, EFW was calculated on the basis of Hadlock's IV formula[48]:

$$\begin{aligned}\mathrm{EFW} = 1.3596 - 0.00386\mathrm{AC} \cdot \mathrm{FL} + 0.0064\mathrm{HC} \\ +0.00061\mathrm{BPD} \cdot \mathrm{AC} + 0.0424\mathrm{AC} + 0.174\mathrm{FL}\end{aligned} \quad (6)$$

Reporting summary

Further information on research design is available in the Nature Portfolio Reporting Summary linked to this article.

Data availability

The data supporting the findings of this study are available in the main text or the Supplementary Information.

Code availability

The code used in this study is available from GitHub (https://github.com/ParkingTom/Autonomous-tracking-algorithm).

References

73. Huang, Z. et al. Three-dimensional integrated stretchable electronics. *Nat. Electron.* **1**, 473–480 (2018).
74. Kempski, K. M., Graham, M. T., Gubbi, M. R., Palmer, T. & Lediju Bell, M. A. Application of the generalized contrast-to-noise ratio to assess photoacoustic image quality. *Biomed. Opt. Express* **11**, 3684–3698 (2020).
75. Wear, K. A. & Shah, A. Nominal versus actual spatial resolution: comparison of directivity and frequency-dependent effective sensitive element size for membrane, needle, capsule, and fiber-optic hydrophones. *IEEE Trans. Ultrason. Ferroelectr. Freq. Control* **70**, 112–119 (2023).
76. Harris, G. R. et al. Hydrophone measurements for biomedical ultrasound applications: a review. *IEEE Trans. Ultrason. Ferroelectr. Freq. Control* **70**, 85–100 (2023).
77. Wear, K. A., Gammell, P. M., Maruvada, S., Liu, Y. & Harris, G. R. Improved measurement of acoustic output using complex deconvolution of hydrophone sensitivity. *IEEE Trans. Ultrason. Ferroelectr. Freq. Control* **61**, 62–75 (2014).
78. Wear, K. A. Hydrophone spatial averaging correction for acoustic exposure measurements from arrays—part I: theory and impact on diagnostic safety indexes. *IEEE Trans. Ultrason. Ferroelectr. Freq. Control* **68**, 358–375 (2021).
79. Szabo, T. L. *Diagnostic Ultrasound Imaging: Inside Out* 2nd edn (Academic Press, 2014).
80. International Electrotechnical Commission. *Medical Electrical Equipment—Part 2–37: Particular Requirements for the Basic Safety and Essential Performance of Ultrasonic Medical Diagnostic and Monitoring Equipment*. Report No. IEC 60601-2-37:2024 (IEC, 2024).

81. Kennedy, A. M. & Woodward, P. J. A radiologist's guide to the performance and interpretation of obstetric Doppler US. *Radiographics* **39**, 893–910 (2019).

Acknowledgements

We thank all pregnant volunteers for their participation. We thank M. Selvaraj, S. La Belle, J. Murillo, H. Valentine, S. Collins, A. Rondoni, E. D'Alberti, I. Noakes, A. Anton, G. James, R. Craik, D. Hedgecott and L. Bozhilova for assistance with subject recruitment and clinical tests. We also thank C. Deane and S. Stock for their discussions and C. Bevan for her public involvement. This work was supported by Wellcome Leap HER01430 (A.G. and S.X.), the National Institutes of Health 1R01EB033464-01 (S.X.) and 1R01HL171652-01 (S.X.) and Accelerating Innovation to Market at University of California, San Diego (S.X.). The content is solely the responsibility of the authors and does not represent the official views of the Wellcome Leap or the National Institutes of Health. G.P. is supported by the Siebel Foundation, Merkin Graduate Fellowship Program and Asan Foundation. A.T.P. is supported by the National Institute for Health Research Oxford Biomedical Research Center. All biological experiments were conducted in accordance with the ethical guidelines of the National Institutes of Health and with the approval of the Institutional Review Board of the University of California, San Diego and the UK Research Ethics Committee. The mention of commercial products, their sources or their use in connection with material reported herein is not to be construed as either an actual or an implied endorsement of such products by the Department of Health and Human Services.

Author contributions

G.P., A.G. and S.X. conceptualized the project. G.P., Y.B., H.H., S.Y.Q., M.Y.L., S.W., P.B., G.G., R.T.W., A.X.R., C.C.F.L., X.X.G., H.J.H., A.Y., M.L. and S.X. developed the UPatch. G.P., X.Y.Y., X.J.C., W.T.Y., R.S.W. and K.A.W. carried out the acoustic safety characterization. G.P., Y.B., H.H., A.R., M.T., J.L., A.T.P., L.I., S.L.C., L.C.L. and A.G. performed the clinical studies. G.P., Y.B., H.H., S.Z., R.S. and S.X. processed and analyzed the data. G.P., H.H., A.L., L.S. and M.S. prepared the figures. G.P. and S.X. wrote the paper. All authors provided constructive and valuable feedback on the manuscript.

Competing interests

S.X. is a cofounder of Softsonics. M.T., L.I. and A.G. are cofounders of Safer Birth. A.T.P. is a senior scientific advisor of Intelligent Ultrasound. The other authors declare no competing interests.

Additional information

Extended data is available for this paper at https://doi.org/10.1038/s41587-026-03140-1.

Supplementary information The online version contains supplementary material available at https://doi.org/10.1038/s41587-026-03140-1.

Correspondence and requests for materials should be addressed to Antoniya Georgieva or Sheng Xu.

Peer review information *Nature Biotechnology* thanks Chi Hwan Lee, Igor Chernyavsky and the other, anonymous, reviewer(s) for their contribution to the peer review of this work.

https://doi.org/10.1038/s41587-026-03140-1

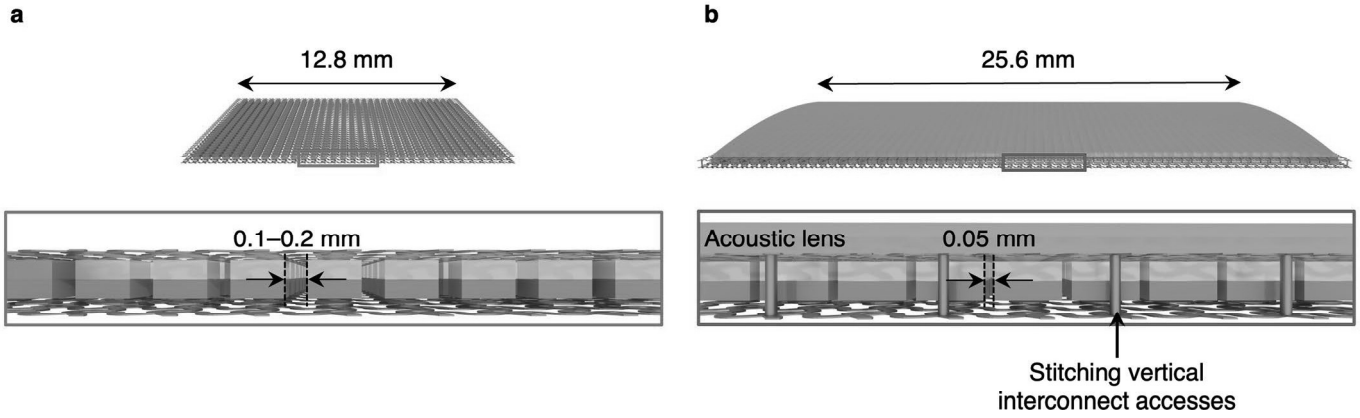

Extended Data Fig. 1 | Hardware comparison of the UPatch with previous wearable ultrasound devices. a, Schematic of a representative previous wearable ultrasound patch developed for cardiac[29] and vascular[49] imaging. Bottom inset is the zoomed-in side view of the transducer array. The maximum aperture was 12.8 mm, and the kerf was 0.1–0.2 mm (ref. 29). Separated liquid metal[29] and copper mesh[49] allowed two-dimensional shielding. **b**, Schematic of the UPatch developed for fetal imaging in this work. Bottom inset is the zoomed-in side view of the transducer array. The aperture was increased to 25.6 mm, providing more than a twofold increase relative to the previous designs. The acoustic lens enhances elevational focusing, reducing the elevational focal beamwidth by 25% and shifting the elevational focal depth from 14 cm to 10 cm to balance resolution across the 20 cm imaging depth of a typical womb. A reduced kerf width of 0.05 mm increases element width, improving signal-to-noise ratio while maintaining a minimal level of crosstalk between adjacent elements. Stitching vertical interconnects accesses with copper mesh enables a three-dimensional soft Faraday cage for improved electromagnetic shielding.

https://doi.org/10.1038/s41587-026-03140-1

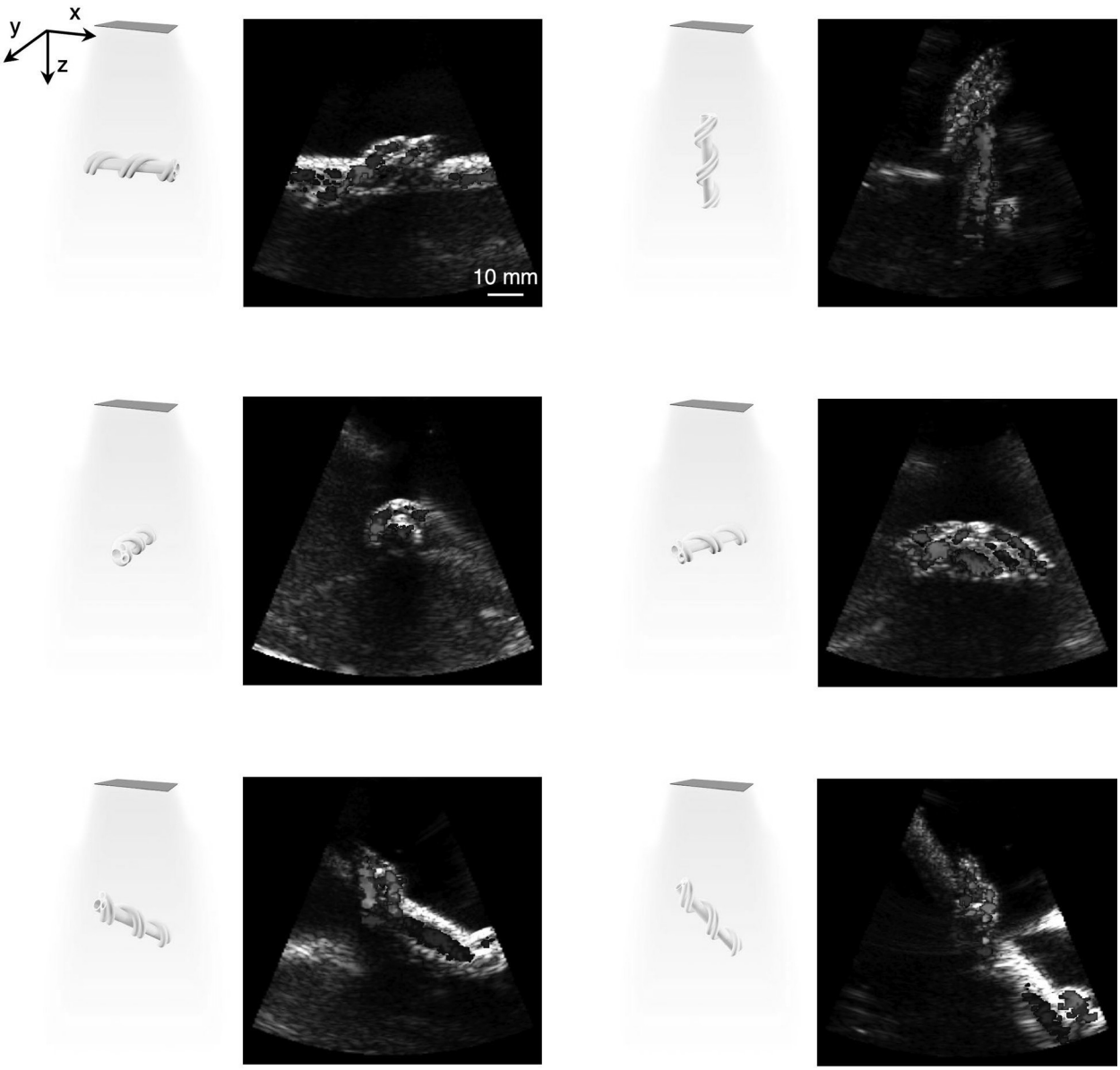

Extended Data Fig. 2 | UPatch imaging of the umbilical cord phantom across various anatomical orientations. The UPatch can image the umbilical cord phantom in diverse spatial configurations. This capability supports the device's application in dynamic in utero environments, accommodating variations in umbilical cord position due to fetal motion and anatomical variability. All images share the same scale bar.

https://doi.org/10.1038/s41587-026-03140-1

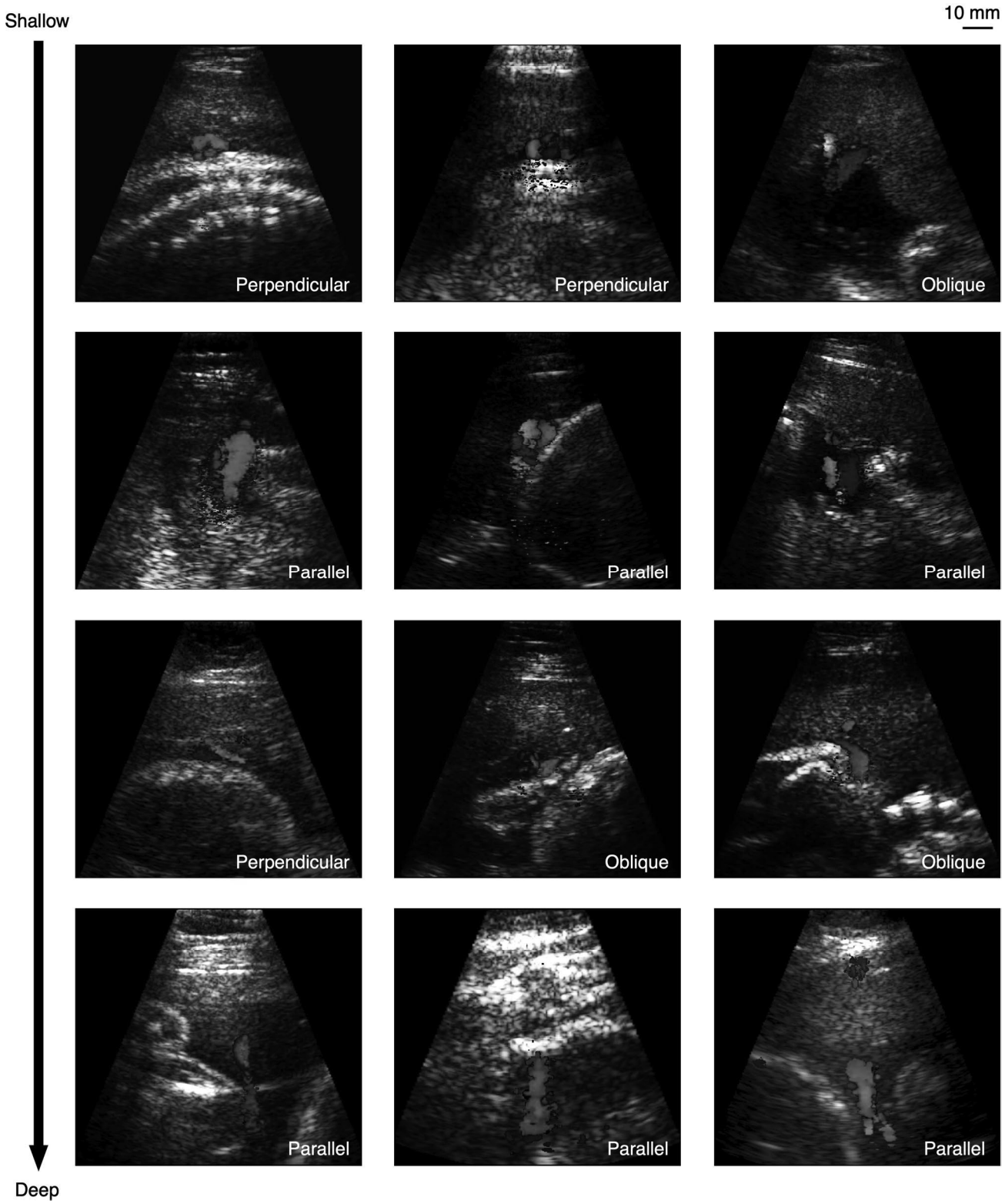

Extended Data Fig. 3 | Duplex images of the umbilical cord. The UPatch can visualize the umbilical cord, including both the umbilical artery and vein, across a range of vessel depths and orientations in pregnant participants. The figure panels are organized to illustrate variations in vessel depth from shallow to deep and differences in vessel orientation relative to the ultrasound beam, including perpendicular, oblique, and parallel cases. All images were acquired by a sonographer specializing in fetal ultrasonography. All images share the same scale bar.

https://doi.org/10.1038/s41587-026-03140-1

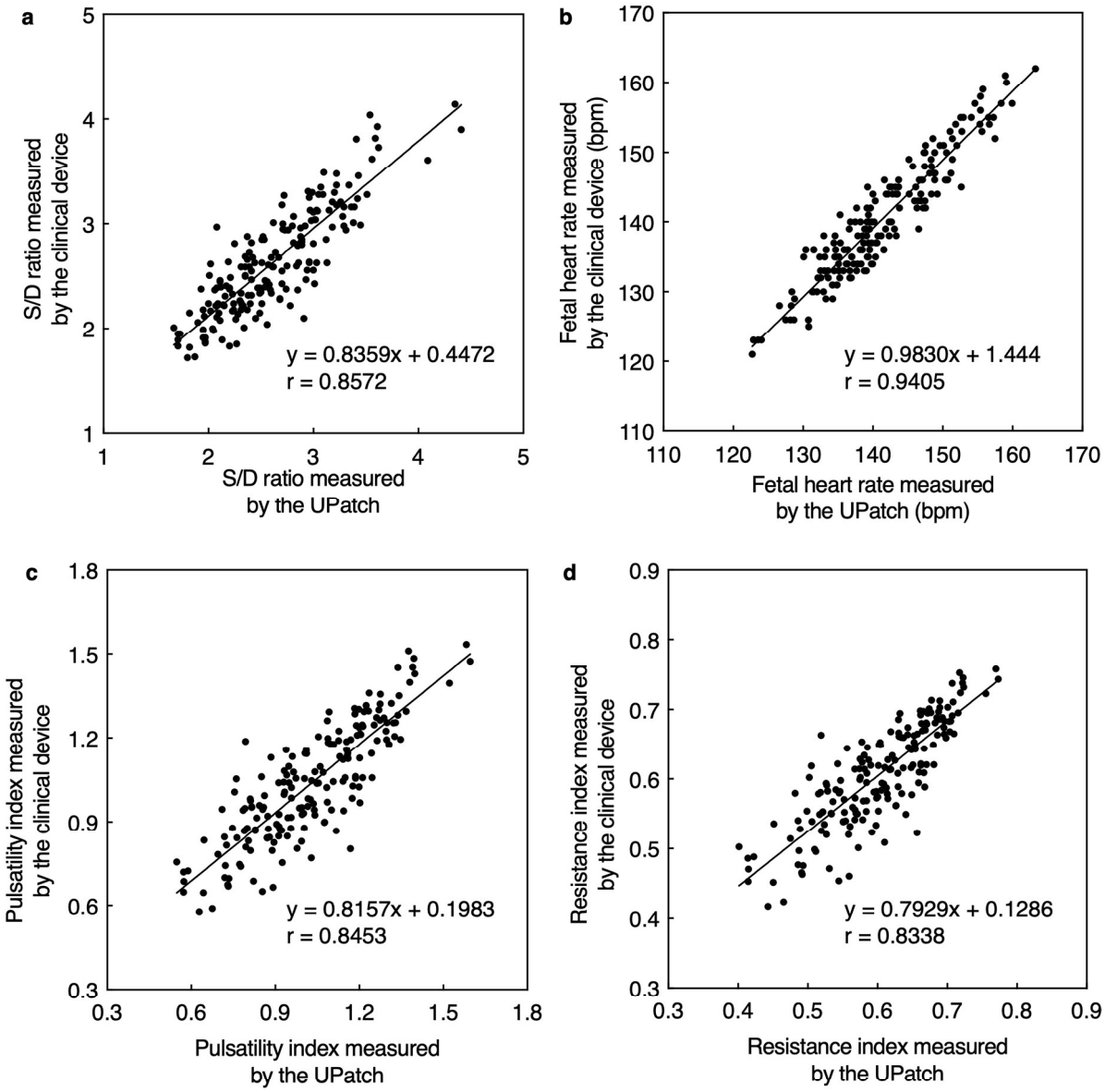

Extended Data Fig. 4 | Correlation analysis of Doppler indices and fetal heart rate. Scatter plots comparing measurements obtained with a clinical ultrasound system (Voluson E10, GE Healthcare) and the UPatch across 62 participants for **a**, systolic-to-diastolic (S/D) ratio, **b**, fetal heart rate, **c**, pulsatility index and **d**, resistance index. Linear regression lines are shown to illustrate agreement across the measurement range. The linear regression equation and Pearson correlation coefficient for each set of data are displayed within each respective plot. r, Pearson correlation coefficient.

https://doi.org/10.1038/s41587-026-03140-1

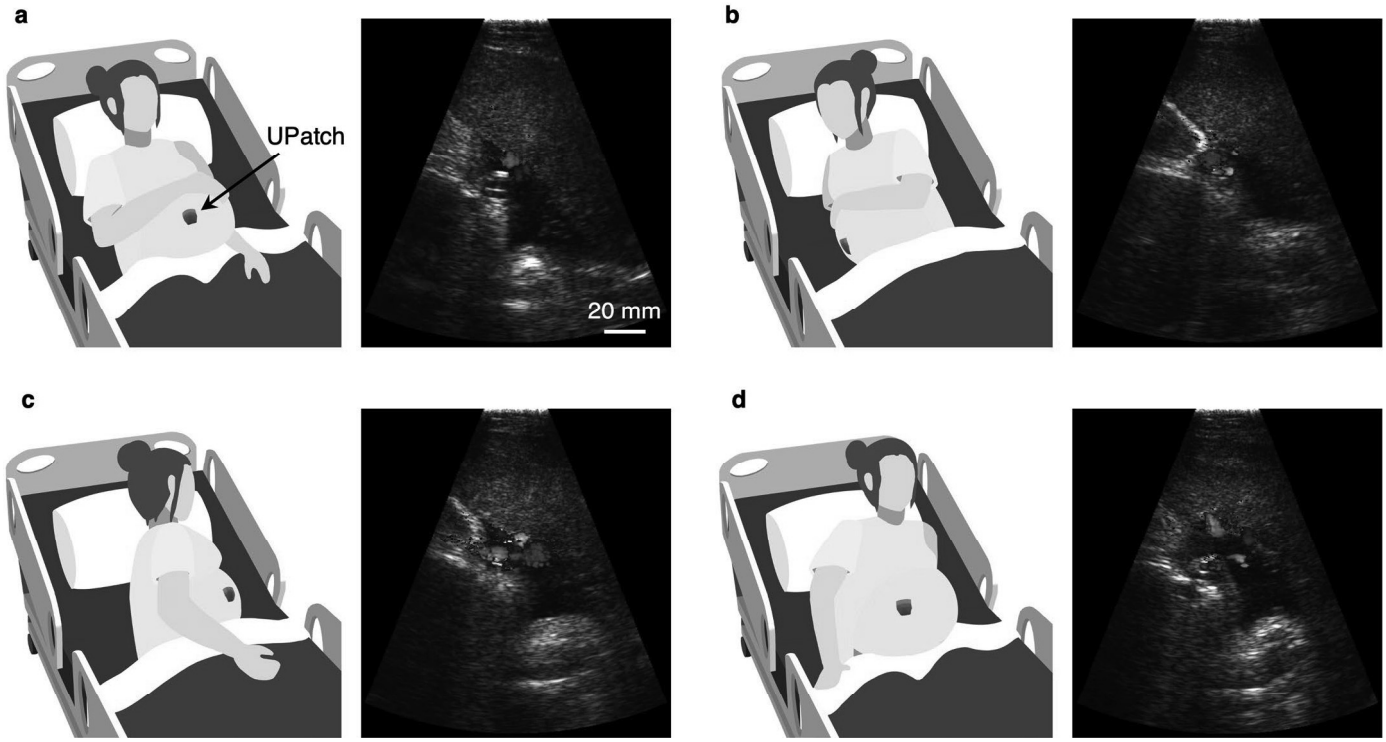

Extended Data Fig. 5 | Duplex imaging of the UPatch across various maternal positions. When positioned to insonate the umbilical cord at the placental cord insertion site, the UPatch maintains reliable signal acquisition during four common postures: **a**, lying supine, **b**, lying on the right side, **c**, lying on the left side and **d**, sitting upright. The images share the same scale bar.

https://doi.org/10.1038/s41587-026-03140-1

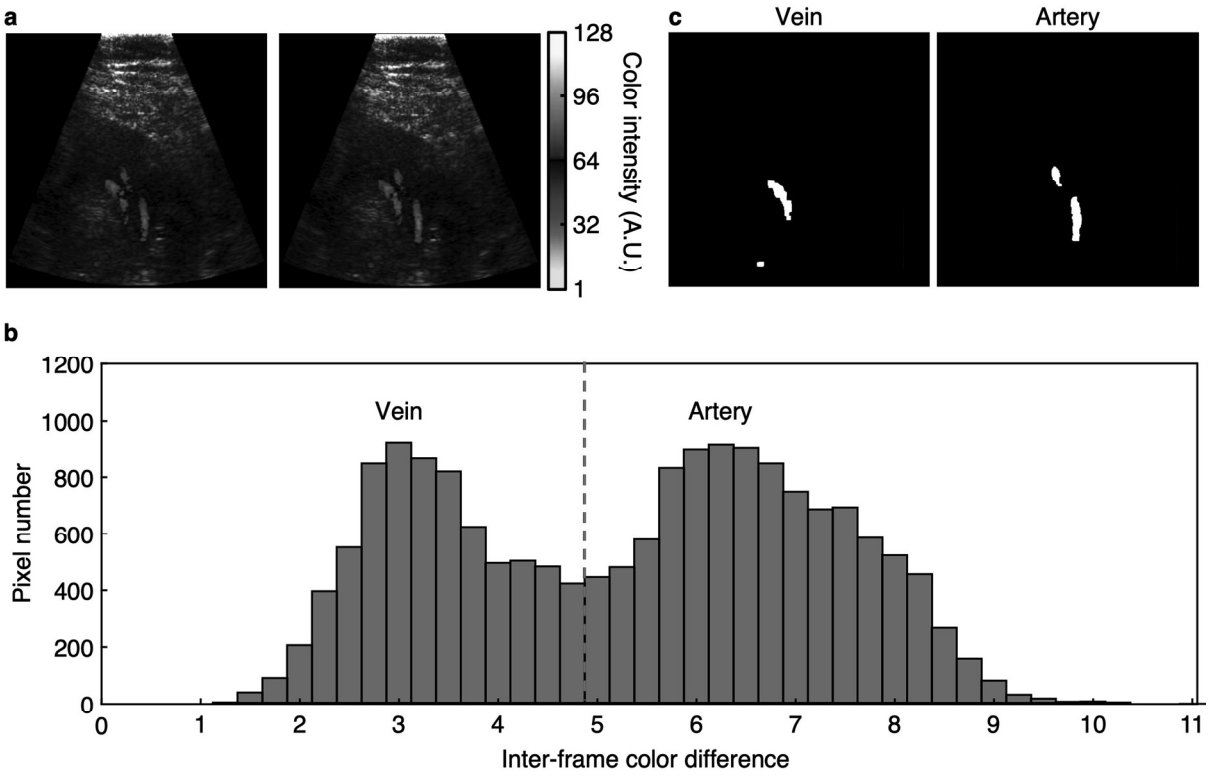

Extended Data Fig. 6 | Segmentation of the umbilical vessels. a, Two consecutive duplex imaging frames showing color Doppler signals in the umbilical vessel region. The images share the same color bar. **b**, Histogram of inter-frame color differences, which is the change in pixel color intensity values between consecutive frames, reflecting temporal fluctuations in blood flow velocity. Due to differences in pulsatility, the artery and vein exhibit distinct inter-frame color differences. The dashed line indicates the threshold value used to differentiate arterial and venous pixels in this study. **c**, Binary segmentation maps of the vein (left) and artery (right), generated by applying the threshold in **b**. The color (cool or warm hues) of the vessel in the image does not affect classification of artery or vein because the algorithm measures the change in color intensity between consecutive frames, not the absolute color.

https://doi.org/10.1038/s41587-026-03140-1

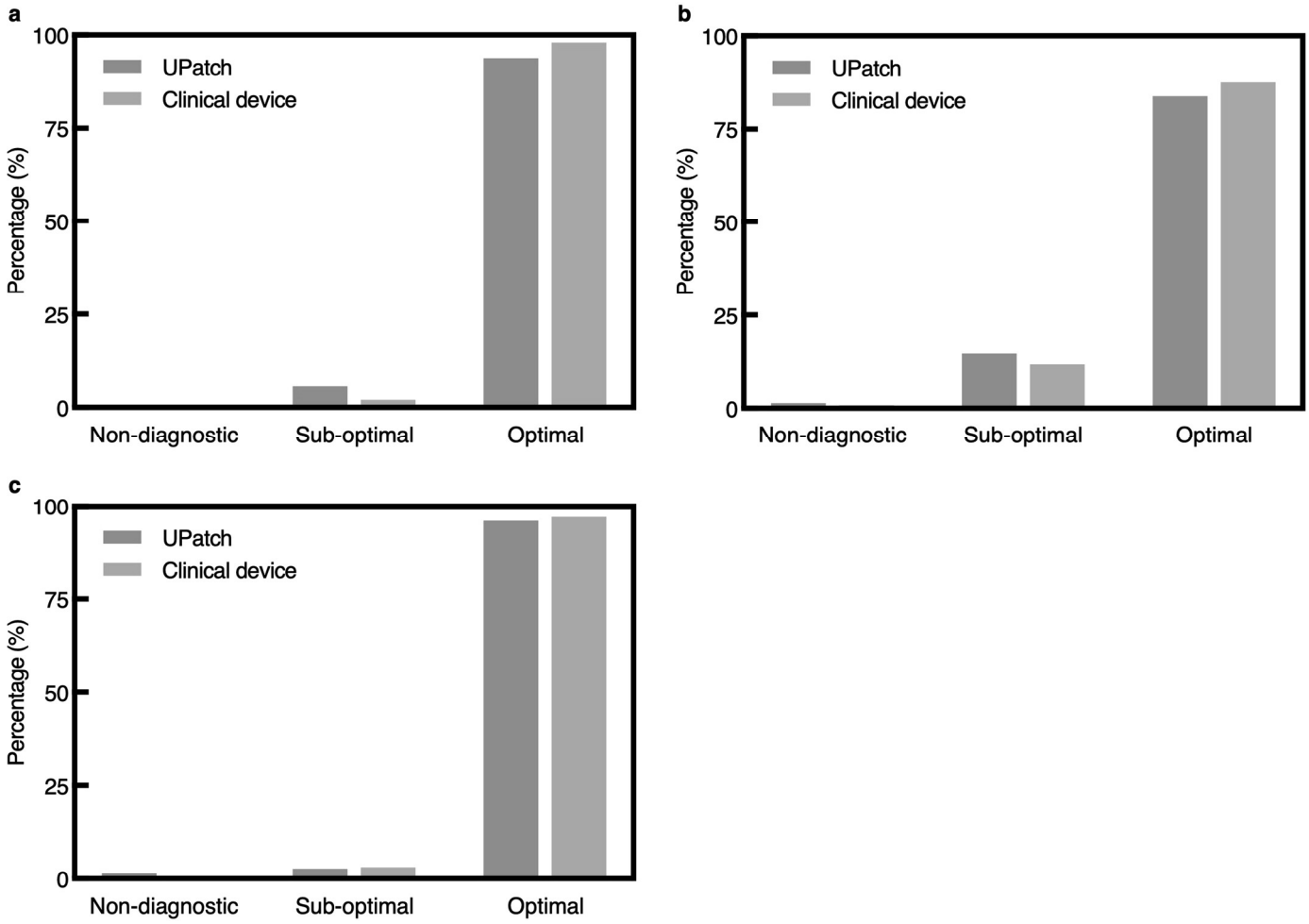

Extended Data Fig. 7 | Sonographer evaluation of the tracking algorithm. Validation by **a**, a sonographer with 30 years, **b**, a sonographer with 8 years, and **c**, a sonographer with 20 years of fetal ultrasonography experience. The tracking algorithm was used to register the sample gate of the umbilical artery in frames collected using a clinical device (Voluson E10, GE Healthcare) and the UPatch. The sonographers evaluated as 'Optimal' for sample gates that are suitable for acquiring spectral Doppler signals, 'Sub-optimal' for sample gates that may yield spectral Doppler signals of low quality, and 'Non-diagnostic' for sample gates that are incapable of providing any spectral Doppler signals. These results demonstrate that the tracking algorithm achieves comparable performance when applied to both the UPatch and the clinical device.

nature portfolio

Corresponding author(s): Sheng Xu

Last updated by author(s): Apr 1, 2026

Reporting Summary

Nature Portfolio wishes to improve the reproducibility of the work that we publish. This form provides structure for consistency and transparency in reporting. For further information on Nature Portfolio policies, see our Editorial Policies and the Editorial Policy Checklist.

Statistics

For all statistical analyses, confirm that the following items are present in the figure legend, table legend, main text, or Methods section.

n/a	Confirmed	
☐	☒	The exact sample size (*n*) for each experimental group/condition, given as a discrete number and unit of measurement
☐	☒	A statement on whether measurements were taken from distinct samples or whether the same sample was measured repeatedly
☐	☒	The statistical test(s) used AND whether they are one- or two-sided *Only common tests should be described solely by name; describe more complex techniques in the Methods section.*
☐	☒	A description of all covariates tested
☐	☒	A description of any assumptions or corrections, such as tests of normality and adjustment for multiple comparisons
☐	☒	A full description of the statistical parameters including central tendency (e.g. means) or other basic estimates (e.g. regression coefficient) AND variation (e.g. standard deviation) or associated estimates of uncertainty (e.g. confidence intervals)
☐	☒	For null hypothesis testing, the test statistic (e.g. *F*, *t*, *r*) with confidence intervals, effect sizes, degrees of freedom and *P* value noted *Give P values as exact values whenever suitable.*
☒	☐	For Bayesian analysis, information on the choice of priors and Markov chain Monte Carlo settings
☒	☐	For hierarchical and complex designs, identification of the appropriate level for tests and full reporting of outcomes
☐	☒	Estimates of effect sizes (e.g. Cohen's *d*, Pearson's *r*), indicating how they were calculated

Our web collection on statistics for biologists contains articles on many of the points above.

Software and code

Policy information about availability of computer code

Data collection	Data collection of the ultrasound signal was carrried out with the Verasonics Vantage 256 system, ONDA ultrasound scanning system (AIMS III hydrophone scanning system), and the radiation force balance (RFB–2000). The code used in this study is available on GitHub (https://github.com/ParkingTom/Autonomous-tracking-algorithm).
Data analysis	Prism 10 and Matlab R2023b

For manuscripts utilizing custom algorithms or software that are central to the research but not yet described in published literature, software must be made available to editors and reviewers. We strongly encourage code deposition in a community repository (e.g. GitHub). See the Nature Portfolio guidelines for submitting code & software for further information.

Data

Policy information about availability of data

All manuscripts must include a data availability statement. This statement should provide the following information, where applicable:

- Accession codes, unique identifiers, or web links for publicly available datasets
- A description of any restrictions on data availability
- For clinical datasets or third party data, please ensure that the statement adheres to our policy

The data supporting the findings of this study are available in the main text or the supplementary information.

Research involving human participants, their data, or biological material

Policy information about studies with human participants or human data. See also policy information about sex, gender (identity/presentation), and sexual orientation and race, ethnicity and racism.

Reporting on sex and gender	All testing was performed exclusively in pregnant women, as defined by the study inclusion criteria.
Reporting on race, ethnicity, or other socially relevant groupings	The information on race/ethnicity was collected in the study design and reported by a table in the manuscript.
Population characteristics	62 subjects for validation study. 52 subjects for continuous monitoring study.
Recruitment	Consenting subjects were recruited randomly.
Ethics oversight	All studies on human subjects in this work were approved by the Institutional Review Board at the University of California, San Diego (IRB #804817) and the UK Research Ethics Committee (23/WA/0032).

Note that full information on the approval of the study protocol must also be provided in the manuscript.

Field-specific reporting

Please select the one below that is the best fit for your research. If you are not sure, read the appropriate sections before making your selection.

☒ Life sciences ☐ Behavioural & social sciences ☐ Ecological, evolutionary & environmental sciences

For a reference copy of the document with all sections, see nature.com/documents/nr-reporting-summary-flat.pdf

Life sciences study design

All studies must disclose on these points even when the disclosure is negative.

Sample size	62 subjects for validation study and 52 subjects for continuous monitoring study.
Data exclusions	No data were excluded.
Replication	The system was evaluated at two independent clinical sites, UC San Diego and the University of Oxford.
Randomization	The subjects were randomly selected.
Blinding	A double-blind evaluation was implemented for the tracking algorithm.

Reporting for specific materials, systems and methods

We require information from authors about some types of materials, experimental systems and methods used in many studies. Here, indicate whether each material, system or method listed is relevant to your study. If you are not sure if a list item applies to your research, read the appropriate section before selecting a response.

Materials & experimental systems

n/a	Involved in the study
☒	☐ Antibodies
☒	☐ Eukaryotic cell lines
☒	☐ Palaeontology and archaeology
☒	☐ Animals and other organisms
☐	☒ Clinical data
☒	☐ Dual use research of concern
☒	☐ Plants

Methods

n/a	Involved in the study
☒	☐ ChIP-seq
☒	☐ Flow cytometry
☒	☐ MRI-based neuroimaging

Clinical data

Policy information about clinical studies

All manuscripts should comply with the ICMJE guidelines for publication of clinical research and a completed CONSORT checklist must be included with all submissions.

Clinical trial registration	This study does not constitute a clinical trial as defined by ICMJE.
Study protocol	The study was conducted under institutional ethics approval with written informed consent from all enrolled pregnant women.
Data collection	Clinical measurements were collected non-invasively using a wearable ultrasound device, with recruitment, consent, and monitoring procedures detailed in the manuscript.
Outcomes	Primary outcomes included correlation accuracy and tracking algorithm performance.

Plants

Seed stocks	*Report on the source of all seed stocks or other plant material used. If applicable, state the seed stock centre and catalogue number. If plant specimens were collected from the field, describe the collection location, date and sampling procedures.*
Novel plant genotypes	*Describe the methods by which all novel plant genotypes were produced. This includes those generated by transgenic approaches, gene editing, chemical/radiation-based mutagenesis and hybridization. For transgenic lines, describe the transformation method, the number of independent lines analyzed and the generation upon which experiments were performed. For gene-edited lines, describe the editor used, the endogenous sequence targeted for editing, the targeting guide RNA sequence (if applicable) and how the editor was applied.*
Authentication	*Describe any authentication procedures for each seed stock used or novel genotype generated. Describe any experiments used to assess the effect of a mutation and, where applicable, how potential secondary effects (e.g. second site T-DNA insertions, mosiacism, off-target gene editing) were examined.*